# UPDATED TSUNAMI INUNDATION MAPS FOR SEWARD AND NORTHERN RESURRECTION BAY, ALASKA

Elena N. Suleimani, J. Barrett Salisbury, and Dmitry J. Nicolsky

# UPDATED TSUNAMI INUNDATION MAPS FOR SEWARD AND NORTHERN RESURRECTION BAY, ALASKA

Elena N. Suleimani, J. Barrett Salisbury, and Dmitry J. Nicolsky

**STATE OF ALASKA**
Mike Dunleavy, Governor

**DEPARTMENT OF NATURAL RESOURCES**
Akis Gialopsos, Acting Commissioner

**DIVISION OF GEOLOGICAL & GEOPHYSICAL SURVEYS**
David L. LePain, State Geologist and Director

**Suggested citation:**
Suleimani, E.N., Salisbury, J.B., and Nicolsky, D.J., 2022, Updated tsunami inundation maps for Seward and northern Resurrection Bay, Alaska: Alaska Division of Geological & Geophysical Surveys Report of Investigation 2022-3, 51 p, 4 sheets. https://doi.org/10.14509/30893

# Contents

# Figures

# Tables

# Appendix

# Map Sheets

Sheet 1: Maximum estimated tsunami inundation for Seward, Alaska

Sheet 2: Maximum estimated tsunami inundation for downtown Seward, Alaska

Sheet 3: Maximum estimated tsunami inundation for Lowell Point, Seward, Alaska

Sheet 4: Maximum estimated tsunami inundation for Fourth of July Creek, Seward, Alaska

# UPDATED TSUNAMI INUNDATION MAPS FOR SEWARD AND NORTHERN RESURRECTION BAY, ALASKA

Elena N. Suleimani[1], J. Barrett Salisbury[2], and Dmitry J. Nicolsky[1]

## Abstract

We re-evaluate potential tsunami hazards for Seward, Alaska by numerically modeling the extent of inundation from tsunami waves generated by hypothetical earthquakes. We define an updated suite of earthquakes—including Tohoku-style megathrust ruptures and complex splay faulting in the upper North American plate from Kodiak Island and Prince William Sound—to calculate vertical seafloor displacements and model resulting tsunami dynamics in Resurrection Bay. A hypothetical earthquake with maximum slip distributed between depths of 0 and 18 km (11.2 mi) results in "worst case" tsunami inundation for Seward. The maximum predicted overland flow depths in the community range from 10 to 25 m (33 to 82 ft), and the currents in community harbors could be as strong as 25 m/sec (48.6 knots). Dangerous wave activity is expected to last for at least 12 hours after the hypothetical worst-case earthquakes. Results presented here are intended to provide guidance to local emergency management agencies for tsunami inundation assessment, evacuation planning, and public education to mitigate future tsunami damage. This report updates the previous assessment of tsunami hazard for Seward published in 2010.

## INTRODUCTION

Subduction of the Pacific plate under the North American plate has resulted in numerous great (M > 8) earthquakes and is the source of locally generated tsunamis in Alaska (Dunbar and Weaver, 2008). During the 20th century, several tsunamis generated by Alaska–Aleutian subduction zone earthquakes have resulted in widespread damage and loss of life in exposed coastal communities throughout the Pacific (Lander, 1996). However, tsunamis originating in the vicinity of the Alaska Peninsula, Aleutian Islands, and Gulf of Alaska are considered near-field hazards and could reach Alaska's coastal communities within minutes of an earthquake. Reducing property damage and loss of life is highly dependent on community preparedness.

On March 27, 1964, the largest earthquake ever recorded in North America struck Southcentral Alaska. This moment magnitude ($M_W$) 9.2 megathrust earthquake, known as the Great Alaska Earthquake (fig. 1), generated the most destructive tsunami in Alaska history and, farther south, impacted the west coast of Canada and the United States (Plafker and others, 1969; Kanamori, 1970; Johnson and others, 1996; Lander, 1996; Fine and others, 2018a, 2018b; Rabinovich and others, 2019). Seward suffered great losses from the earthquake and the ensuing tsunami. In addition to the major tectonic tsunami generated by ocean-floor displacement in the Gulf of Alaska, numerous local tsunamis were generated by landslides in coastal Alaska during the Great Alaska Earthquake (Lander, 1996). Landslide-generated tsunamis arrived almost immediately after the earthquake shaking, leaving no time for warning or evacuation.

[1]Alaska Earthquake Center, Geophysical Institute, University of Alaska, P.O. Box 757320, Fairbanks, Alaska 99775-7320.
[2]Alaska Division of Geological & Geophysical Surveys, 3354 College Rd., Fairbanks, Alaska 99709-3707.
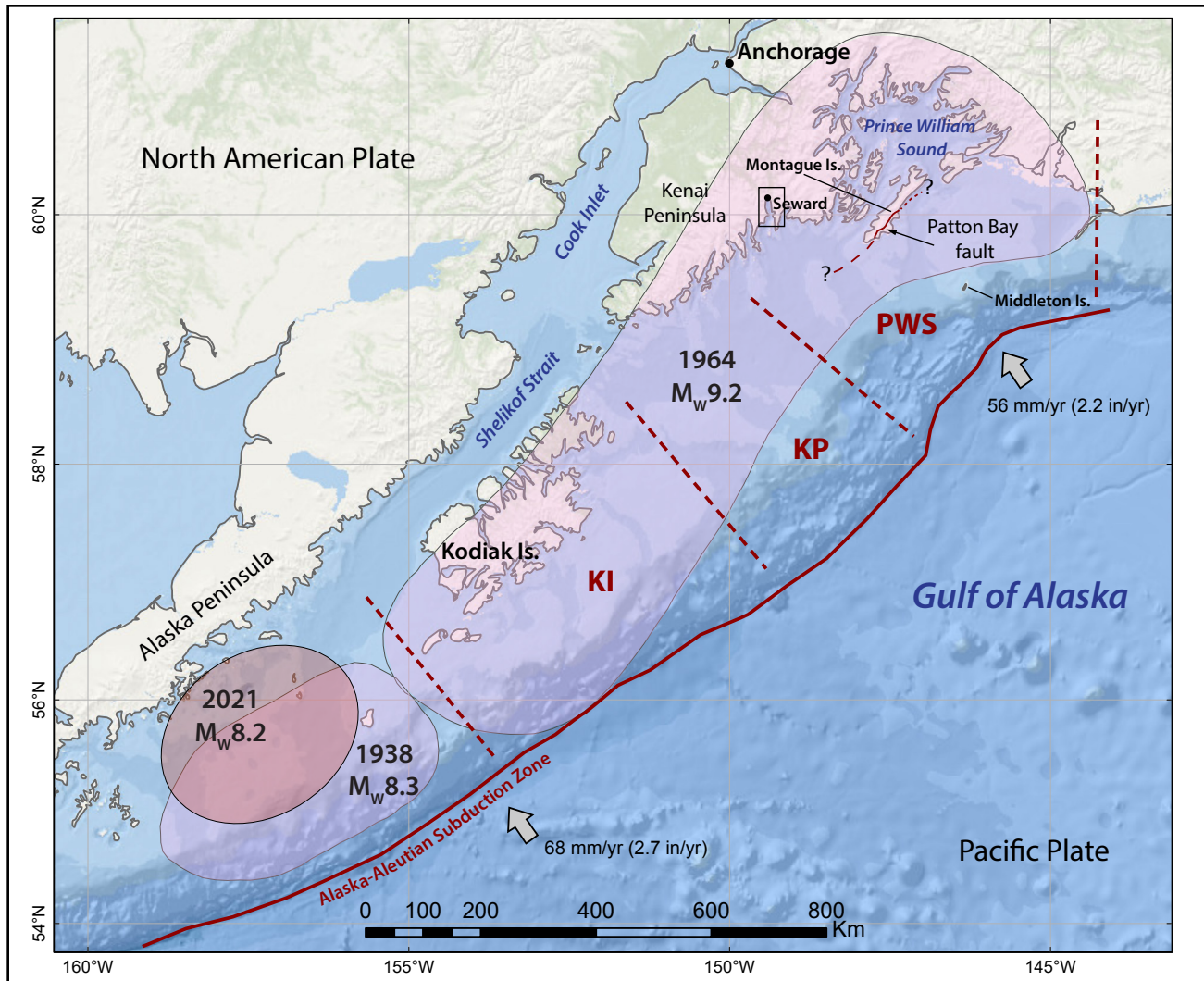
**Figure 1.** Map of Southcentral Alaska, showing the location of Seward on the Kenai Peninsula, and the rupture zones of the 1938, 1964, and 2021 Alaska–Aleutian megathrust earthquakes (shaded areas). KI = Kodiak Island segment; KP = Kenai Peninsula segment; PWS = Prince William Sound segment. Black rectangle around Seward represents study area.The Patton Bay fault is shown by solid, dashed, and dotted lines where it is mapped with certainty, approximately, and inferred, respectively

Of the 131 fatalities associated with this earthquake, 122 were caused by tsunami waves (Lander, 1996). Despite this relatively recent $M_W$ 9.2 earthquake, the region still has high potential for future large earthquakes and it is only a matter of time before another devastating tsunami occurs (Kirby and others, 2013). Thus, estimating the potential flooding of the coastal zone in the next tsunami is an essential component of the preparedness process.

This report updates the previously published tsunami hazard assessment for Seward and northern Resurrection Bay, Alaska (Suleimani and others, 2010). Combined with high-resolution continuous global positioning system (GNSS and GPS) measurements along the southern Alaska coast, the tsunami disasters of 2004 in Indonesia and 2011 in Japan have helped improve our understanding of complex earthquake source mechanisms. Consequently, we include new potential earthquake sources in our updated tsunami analysis to develop the worst-case credible tsunami scenarios for Seward.

The tsunami inundation map for Seward and northern Resurrection Bay described in this report

represent the results of a continuous, combined effort of state and federal agencies to mitigate tsunami damage in coastal Alaska. The intended audience of this report consists of scientists, engineers, and community planners interested in an applied approach to developing tsunami inundation and evacuation maps. Digital data and documentation provided with the report enable technical users to explore the range of possible tsunami inundation for potential events. We use a deterministic approach for our earthquake and tsunami hazard modeling, which is distinctly different from the probabilistic tsunami hazard analysis used in projects with different objectives, such as land-use planning or insurance estimates (Geist and Parsons, 2006). We are less concerned about the probability that an earthquake of a certain magnitude will occur in a given amount of time and are more focused on the community-specific tsunami inundation that might result from the largest hypothetical, yet scientifically plausible earthquake scenarios. The methodologies used to develop tsunami inundation maps are described in detail in multiple publications and are not reviewed in this report. Refer to Suleimani and others (2016) for a complete description of the process.

## PROJECT BACKGROUND: REGIONAL AND HISTORICAL CONTEXT
### Setting

The town of Seward (population of 2,509) is near the northwest corner of Resurrection Bay, about 200 km (125 mi) south of Anchorage (figs. 1 and 2). The following information is from the Alaska Community Database maintained by the State of Alaska Division of Community and Regional Affairs of the Department of Commerce, Community, and Economic Development (DCCED/DCRA, 2015).

During the construction of the Alaska Railroad between 1915 and 1923, Seward became an ocean terminus and supply center for Interior Alaska. The economy of Seward has long been dominated by transportation and supply services. At the time of the 1964 earthquake, the economy of Seward was based on shipping, and was heavily dependent on the city's railroad, harbor, and port operations. Seward has grown considerably since the 1964 earthquake. Its economy is more diversified and includes tourism, commercial fishing, and fish processing, as well as oil and gas development. Still, much of the economic activity and infrastructure is located on or near the coast, ports, and harbors. As an ice-free harbor, it is an important supply center for Interior Alaska, and it is a port for the state ferry system.

Seward was severely impacted by the March 27, 1964, earthquake and tsunami waves. The economic base of the town was devastated, due largely to the loss of harbor facilities from the earthquake and resultant slope failures offshore the Seward waterfront (Lemke, 1967). Both local landslide-generated waves and distant tectonically generated waves inundated the Seward shoreline and caused tremendous damage (Lemke, 1967). Thirteen people were killed and five injured in Seward as a combined result of the earthquake and tsunami waves. Eighty-six houses were destroyed and 269 were heavily damaged. Refer to Suleimani and others (2010) for an overview of regional seismotectonics and detailed description of events in Seward on March 27, 1964.

Other tsunamis reached Seward in the past, as documented by the National Centers for Environmental Information/World Data Centers (NCEI/WDS) Global Historical Tsunami Database (www.ngdc.noaa.gov/hazard/tsu_db.shtml) and Lander (1996). Table 1 summarizes all historically recorded tsunami events that reached Seward and resulted in a wave height of 0.1m (0.3ft) or larger.

## Landslide-Generated Tsunami Hazards

On March 27, 1964, strong ground shaking triggered several underwater slides in Resurrection Bay within seconds of the onset of the earthquake. The locally generated waves flooded town two minutes later, causing devastation and loss of life. An overview of landslide-generated tsunami

hazard in Resurrection Bay is given in Suleimani and others (2009, 2010, 2011). In the previously published report on tsunami hazards in northern Resurrection Bay (Suleimani and others, 2010), we performed numerical modeling of the March 27, 1964, local tsunamis generated by underwater slope failures during the Great Alaska earthquake, as well as tsunamis that could be generated by hypothetical
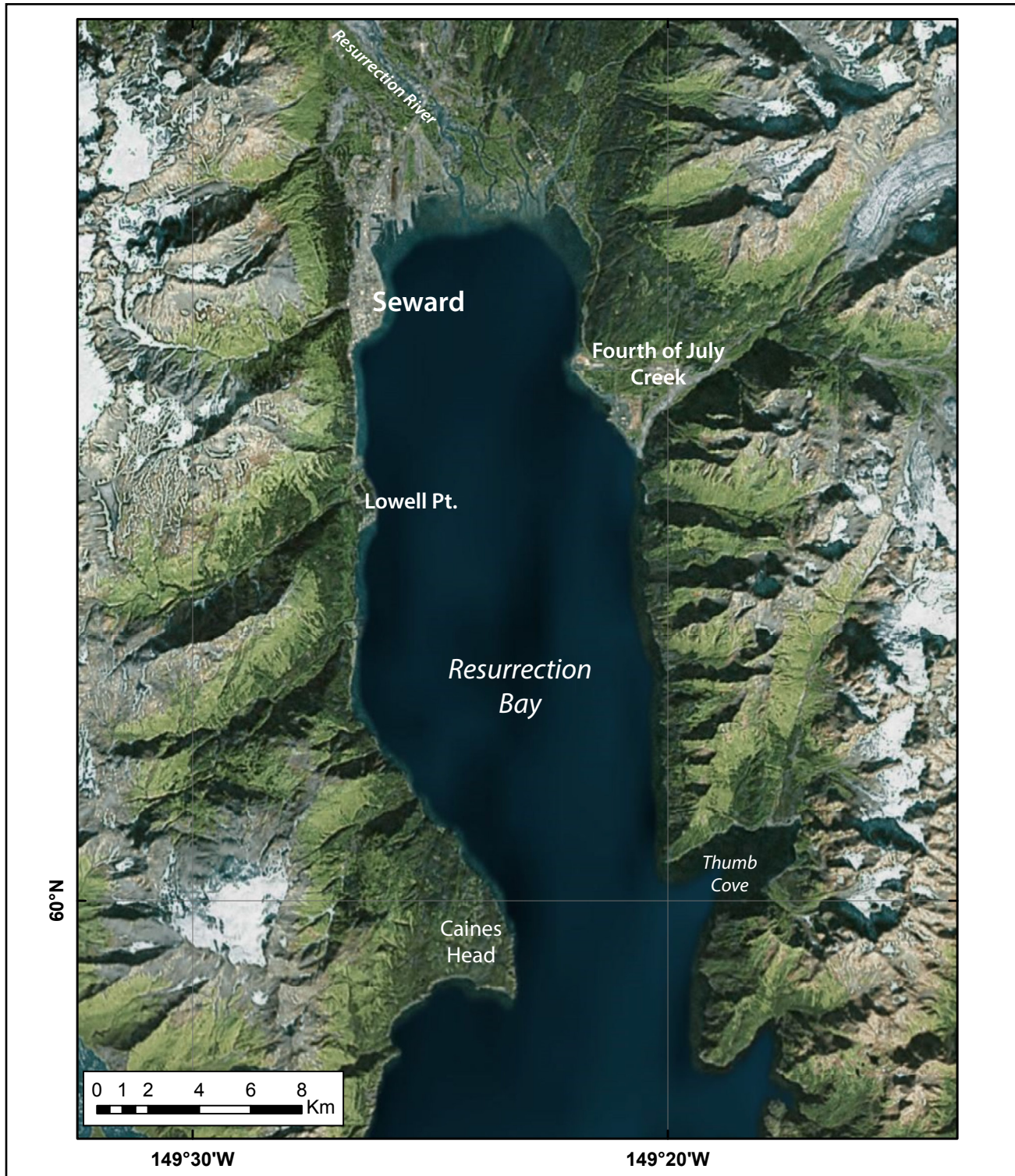


**Figure 2.** Aerial photograph of Resurrection Bay.

**Table 1.** Tsunami effects at Seward; data from the National Geophysical Data Center Global Historical Tsunami Database (NCEI/WDS) and comments from Lander (1996).

| Date (mm/dd/yyyy) | Magnitude ($M_W$) | Origin | Maximum water height, m (ft) | Comments |
|---|---|---|---|---|
| 03/02/1933 | 8.4 | Japan | 0.1 (0.3) | |
| 04/01/1946 | 8.6 | Alaska Peninsula | 0.1 (0.3) | |
| 03/09/1957 | 8.6 | Kamchatka, Russia | 0.2 (0.6) | |
| 05/22/1960 | 9.5 | Chile | 0.7 (2.3) | |
| 03/28/1964 | 9.2 | Gulf of Alaska | 8.3 (27.2) | Disastrous to town, waterfront, boats and railroad. $14.6 million in damage. Section of waterfront slid into bay. 12 deaths due to combined effect of local and main tsunamis. Cannery destroyed. |
| 11/30/1987 | 7.9 | Gulf of Alaska | 0.1 (0.3) | |
| 02/27/2010 | 8.8 | Chile | 0.4 (1.3) | |
| 03/11/2011 | 9.1 | Japan | 0.47 (1.5) | |
| 09/16/2015 | 8.3 | Chile | 0.1 (0.3) | |
| 01/23/2018 | 7.9 | Gulf of Alaska | 0.1 (0.3) | |

slope failures. We analyzed bathymetric differences in Resurrection Bay derived from pre- and post-1964 depth measurements (Haeussler and others, 2007), which indicated four major areas in upper Resurrection Bay where sediment accumulated since 1964. Based on this data, we developed hypothetical landslide scenarios and performed numerical modeling of tsunami waves. Since the publication of the report in 2010, we have not received any additional data on sediment accumulation in Resurrection Bay that could change our assessment of landslide tsunami hazard in Seward.

## METHODOLOGY AND DATA
## Grid Development and Data Sources

We use a series of nested computational grids on the southeastern coast of the Kenai Peninsula to generate detailed maps of potential tsunami inundation triggered by local and distant earthquakes. The coarsest grid, with 2-arc-minute (approximately 2 km [~1.2 mi]) resolution, spans the central and northern Pacific Ocean. We used three intermediate grids between the coarsest- and highest-res-

olution grids (table 2; fig. 3). The highest-resolution grid (level 4, shaded rectangle in fig. 3) covers Resurrection Bay. The spatial resolution of the level 4 grid, with cell dimensions of about 13.7 × 13.7 m (45 × 45 ft), satisfies National Oceanic and Atmospheric Administration (NOAA) minimum recommended requirements for computation of tsunami inundation (National Tsunami Hazard Mapping Program [NTHMP], 2010). The high-resolution level 4 grid of combined bathymetric, topographic, and shoreline digital datasets was developed by Labay and Haeussler (2008).

The map sheets of potential tsunami inundation included in this report show the maximum composite extent of inundation for all considered tsunami scenarios, and the maximum composite flow depths over dry land. The composite values are calculated as follows: for each tsunami scenario, the tsunami flow depth is computed at each grid point and at every time step during the tsunami propagation time the maximum value is kept; then we compute the composite maximum flow

**Table 2.** Nested grids used to compute propagation of tsunami waves generated in the Pacific Ocean to Resurrection Bay. The high-resolution grid is used to compute the inundation. Note that the grid resolution in meters is not uniform: the first dimension is the longitudinal grid resolution and the second is the latitudinal resolution.

| Grid name | Resolution | | West–East boundaries | South–North boundaries |
| --- | --- | --- | --- | --- |
| | arc-seconds | feet (meters) | | |
| Level 0, Northern Pacific | 120 × 120 | ≈6,611 x 12,139 (2,015 × 3,700) | 120°00'00" E – 100°00'00" W | 10°00'00" N –65°00'00" N |
| Level 1, South-central Alaska | 24 × 24 | ≈ 1,322 x 2,428 (403 × 740) | 156°00'00" W –145°00'00" W | 55°00'00" N –62°00'00" N |
| Level 2, Coarse resolution, Resurrection Bay | 8 × 8 | ≈ 407 x 810 (124 × 247) | 149°59'56" W – 149°00'04" W | 59°30'04" N – 60°09'56" N |
| Level 3, Fine resolution, Resurrection Bay | 8/3 × 8/3 | ≈ 135 x 269 (41 × 82) | 149°37'27" W – 149°14'17" W | 59°42'41" N – 60°07'35" N |
| Level 4, High resolution, Resurrection Bay | 8/9 × 1/2 | ≈ 45 x 45 (13.7 x 13.7) | 149°27'28" W – 149°16'46" W | 59°57'02" N – 60°09'22" N |

depth from all considered scenarios by choosing the maximum value for each grid point among all scenarios. The same methodology is used to calculate the composite extent of tsunami inundation. The calculated extent of inundation accounts for coseismic deformation in the communities.

## Numerical Model of Tsunami Propagation and Runup

To estimate tsunami propagation and runup in Resurrection Bay, we used the same numerical modeling techniques as previous Alaska tsunami inundation studies (for example, Suleimani and others, 2010, 2013, 2015, 2016; Nicolsky and others, 2011, 2013, 2014, 2015). All hypothetical tsunami simulations were conducted using the bathymetric/topographic data corresponding to the Mean Higher High Water (MHHW) tide level in Resurrection Bay. Because the numerical model of tsunami propagation and runup does not dynamically simulate interaction of tides and tsunami waves, we use a conservative approach and assume that all simulated tsunamis arrive during high tides and with consideration to tectonic land-level changes (i.e., subsidence or uplift) caused by hypothetical earthquakes.

The numerical modeling results presented in this report are relevant for existing sea level conditions and do not account for changes in water levels caused by global sea level rise, regional tectonic processes, and isostatic rebound. Even though the report on global sea level changes for 2050 and 2100 by the Intergovernmental Panel on Climate Change (Oppenheimer and others, 2019) predicts global sea level rise, rapid regional uplift in southern Alaska caused by ice loss contributes to negative sea level changes in the region (Larsen and others, 2004; Shirzaei and others, 2021).

## TSUNAMI SOURCES

In general, all the great historic earthquakes along the Alaska–Aleutian subduction zone occurred on the megathrust—the fault, or contact surface, between the subducting Pacific plate and the overriding North American plate (fig. 1). Friction between the two converging plates generally keeps them stuck, or "locked" together at the edges. Relative plate motion causes energy to accumulate at the plate boundaries and this energy is eventually released during sudden slip in an earthquake. It is theorized that the strain energy primarily accumulates in the locked, or coupled, regions of the

megathrust where friction on the fault is greatest. Our goal is to determine the segments of the interface that are most likely to rupture in the next large or great earthquake.

The Kenai Peninsula is located at the eastern end of the Alaska–Aleutian subduction zone (fig. 1), directly above the plate interface (or megathrust) that is the source of great (M > 8) historical earth-

quakes in southern Alaska. Motion of the Pacific plate relative to the North American plate in the Kenai Peninsula (KP) region reaches ~5.6 cm/year (~2.2 in/year; Freymueller and others, 2008). At the northeast end of the megathrust near Prince William Sound (PWS), this process is complicated by the subduction of the relatively buoyant Yakutat block along with the Pacific plate. This results in
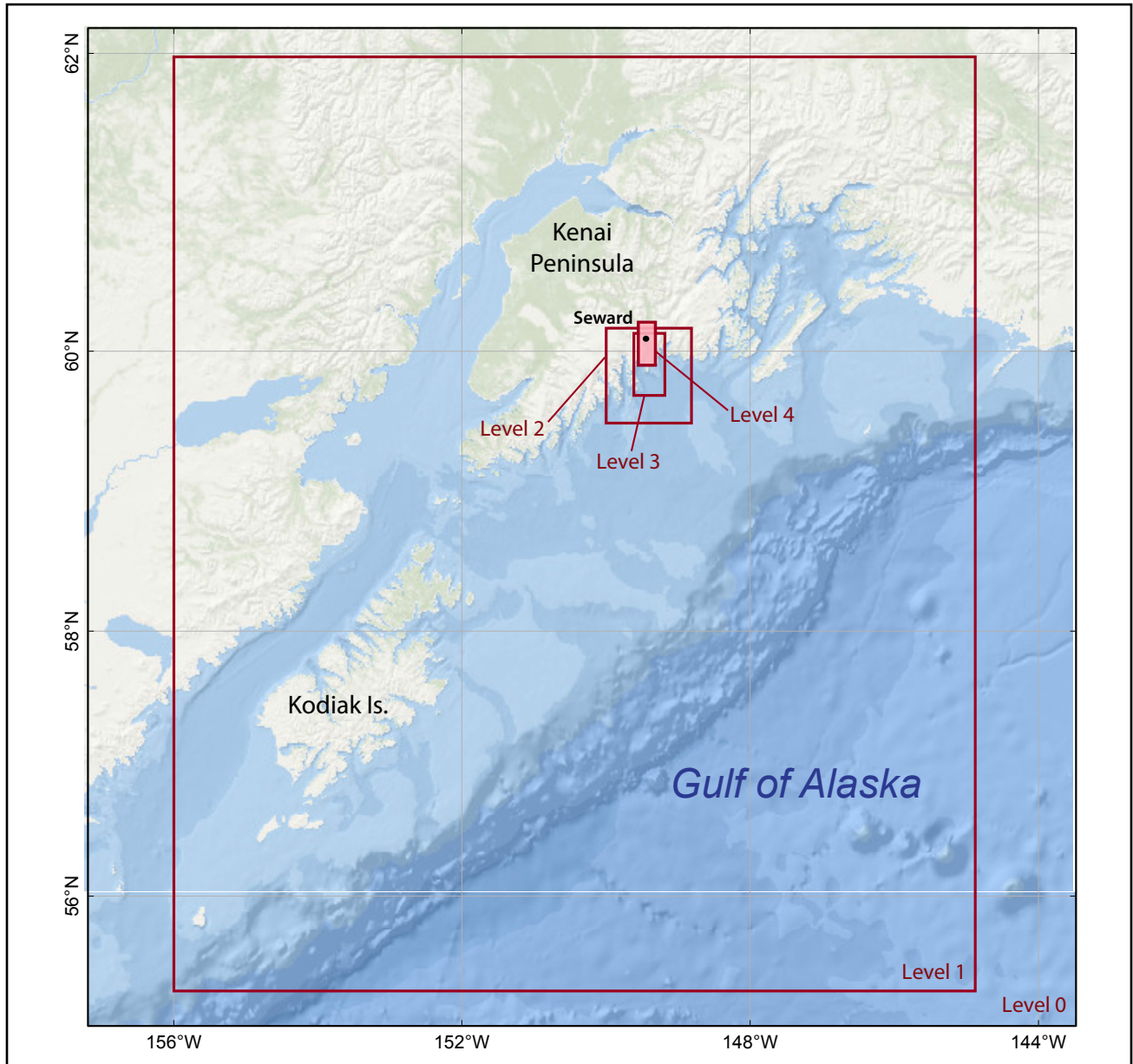


**Figure 3.** Nesting of the levels 0–4 bathymetry/topography grids for numerical modeling of tsunami propagation and runup in upper Resurrection Bay. Each embedded grid is outlined by a red rectangle. Note that we extended the level 4 grid northward to accommodate extensive inundation over dry land but the water domain of the level 4 grid is completely contained by the level 3 grid.

a wide and shallow plate interface under PWS, which is locked during the interval between great earthquakes (Savage and others, 2015).

Using seismic waveform data, Christensen and Beck (1994) showed that there were two areas of high moment release during the 1964 Great Alaska Earthquake, representing the two major asperities of the 1964 rupture zone: the PWS asperity with an average slip of 18 m (59 ft), and the Kodiak Island (KI) asperity with an average slip of 10 m (33 ft) (fig. 5). The KP segment separates these two areas of high slip in the 1964 earthquake. The results of joint inversion of tsunami and geodetic data from the 1964 earthquake (Johnson and others, 1996) also suggest two areas of high moment release. Zweck and others (2002) used a three-dimensional elastic dislocation model to demonstrate that the GPS data in southern Alaska can be satisfied by the presence of locked areas near southwest PWS and southwest Kodiak Island. They found that locked areas correspond to the PWS and KI asperities that ruptured in 1964, and that the locked regions repeat from one earthquake cycle to another. Subsequent studies have shown that the PWS asperity is on the Yakutat-North American megathrust whereas the KI asperity is on the Pacific-North American megathrust, indicating that the 1964 event ruptured across both the Yakutat and Pacific interfaces (Ferris and others, 2003; Eberhart-Phillips and others, 2006; Worthington and others, 2010, 2012; Gulick and others, 2013). Recently, Elliott and Freymueller (2020) used an updated GPS dataset to constrain a tectonic block model to study coupling variations at the eastern part of the Alaska–Aleutian subduction zone. The model predicted strong coupling beneath Prince William Sound and Kodiak Island, and partial coupling under the Kenai Peninsula. They suggested that the areas of high slip in 1964 correspond to areas of strong interseismic coupling, and the slow slip events in the western part of the Kenai Peninsula are above the transition between the Yakutat and Pacific slabs, where the model predicts partial coupling.

The geometry of the plate interface varies along the strike of the plate boundary between PWS and Kodiak Island. The dip of the subducting plate steepens from about 3–4° in the PWS region, where the plate interface is the contact between the North America plate and Yakutat block, to about 8° near Kodiak Island, where the plate interface is between the North America plate and Pacific plate (Cohen and Freymueller, 2004). Because the width of the plate interface around PWS and the Kenai Peninsula is quite large (measured in the down-dip direction, e.g., fig. 4), earthquakes in this area do not necessarily rupture the whole interface every time. In the PWS segment, the plate interface is locked and accumulates strain between the trench and depths of about 20–25 km (12.4–15.5 mi) (Freymueller and others, 2008). Locating the updip limit of the locked zone near the Kenai Peninsula and PWS is hindered by the lack of geodetic data close to the Aleutian trench, and this zone is essentially unconstrained by land-based geodetic data. Because we do not yet have seafloor GPS/acoustic measurements to constrain the behavior of the uppermost portion of the plate interface, it was necessary to perform additional steps to construct maximum credible earthquake (and therefore tsunami) scenarios for Seward.

Recent studies comparing the Alaska and Tohoku, Japan, tectonic margins (Kirby and others, 2013) suggest that there are several key geologic similarities between the two areas and that a hypothetical rupture might propagate to shallow depths on the Alaska–Aleutian megathrust, in a process similar to what took place during the $M_W$ 9.0 Tohoku earthquake. Therefore, in our scenarios, we include earthquakes that rupture the shallow locked zone. Additionally, we conduct a sensitivity study to determine what effect the down-dip location of a rupture has on tectonic subsidence, uplift, and resulting tsunami waves. We then apply the results of the sensitivity study to construct the maximum credible scenarios.

## Sensitivity Study

Earthquake ruptures with slip at different depths have different wave-generating potential,

result in different distributions and amounts of subsidence and uplift in coastal communities, and therefore result in different tsunami and permanent flooding characteristics. The point of the sensitivity study is to determine the most dangerous location on the megathrust for a hypothetical earthquake to occur. We use the USGS SLAB2 model of the Alaska–Aleutian plate interface developed by Hayes (2018). Like the plate interface model used by Zweck and others (2002), the SLAB2 plate interface model exhibits a relatively shallow dip beneath Prince William Sound and the Kenai Peninsula until it reaches a depth of 30 km (18.6 mi), at which point it steepens (fig. 4). This deep area also corresponds

to the unlocked or weakly coupled part of the plate interface (Zweck and others, 2002).

The plate interface is discretized into a mesh of rectangles ranging from 1 to 6 km (0.6 to 3.7 mi) in the along-strike direction of the plate interface, with denser discretization in its shallow part (fig. 4). The upper and lower edges of each rectangle coincide with depth contours of the plate interface that are spaced at 0.5 km (0.3 mi), with spacing of 0.25 km (0.16 mi) at the shallowest part of the plate interface. The rectangles, called subfaults, are later used to compute coseismic ground deformation (Okada, 1985). Using this discretization
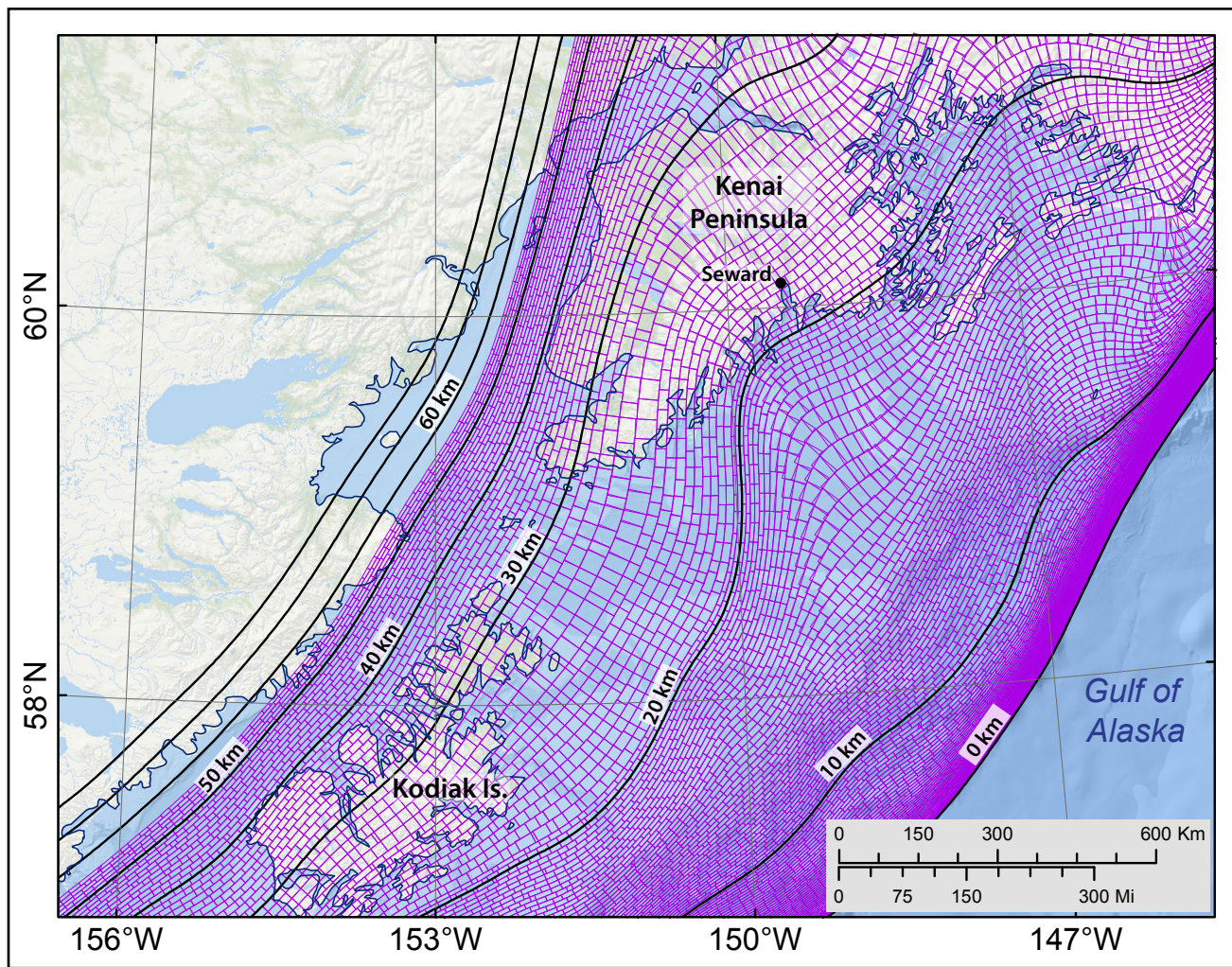


**Figure 4.** Discretization of the plate interface used to compute the coseismic vertical displacements with formulae developed by Okada (1985). Black lines mark depth contours (in kilometers) of the plate interface and the purple rectangles represent individual pieces of the plate considered by the model.

of the plate interface, we model potential earthquake scenarios by prescribing a general pattern of slip distribution in the proposed rupture, then computing the slip at the center of each subfault using seismic moment as a constraint.

The PWS area of the Alaska–Aleutian megathrust is one of the two large segments of the 1964 rupture zone with a very wide locked region (200–250 km [124.3–155.3 mi] wide in the downdip direction), but the detailed shape of the locked region is uncertain (Freymueller and others, 2008). The KP segment (fig. 1) is currently creeping, but it was shown by Kelsey and others (2015) that it can rupture independently of the PWS segment that is presently locked. The authors used paleoseismic data from two coastal sites on Kenai Peninsula that show the evidence of two subduction zone earthquakes that predate the 1964 earthquake. The penultimate Kenai earthquake of AD 1530–1840 did not rupture the PWS segment, showing that earthquakes in the eastern part of the Alaska–Aleutian subduction zone can propagate through multiple segments with varying degree of coupling, and that presently locked areas do not necessarily rupture in all past earthquakes.

Earthquake ruptures with slip at different depths result in different tsunami and permanent flooding characteristics. Therefore, we develop four different slip cases (cases A–D) for $M_W$ 9.0 earthquakes that could occur in the partially locked segment of the megathrust in the area between PWS and Kodiak Island (Freymueller and others, 2008) and calculate vertical seafloor deformations associated with each case (fig. 5). The slip distribution for all four cases is uniform in the along-strike direction with tapering at the ends of the rupture. The assumed slip distribution is consistent with earthquake source scenarios used by other tsunami modeling studies (for example, Butler, 2014; USGS SAFRR scenario, www2.usgs.gov/natural_hazards/safrr/projects/tsunamiscenario.asp). Between any two consecutive cases, the hypothetical rupture is offset by about 10 km (6.2 mi) in the downdip direction: case A corresponds to a shallow surface-breaching rupture with maximum amount of slip located close to the trench; cases B, C, and D correspond to ruptures with maximum slip roughly centered at 10 km (6.2 mi), 20 km (12.4 mi), and 30 km (18.6 mi) depths, respectively.

Simulated water levels at Seward vary considerably according to different slip distributions (fig. 6). The time series indicate that the rupture at 10 km (6.2 mi; case B) results in the highest wave amplitude, followed by case A, the shallow surface-breaching rupture. Case C, the rupture at 20 km (12.4 mi) depth, results in smaller wave amplitudes, but with an earlier wave arrival. The deep rupture represented by case D produces sizable coseismic uplift along the southern shore of the Kenai Peninsula. As a result, the bay seabed and surrounding land surfaces are relatively higher after the earthquake and the arriving waves effectively have much smaller amplitudes.

Based on these results, we develop hypothetical ruptures with maximum slip in the 0–20 km (0–12.4 mi) depth range (cases A–C). As in Nicolsky and others (2016), we develop maximum credible scenarios for Seward by allowing up to 35 m (115 ft) of slip in the deep and intermediate sections of the Alaska–Aleutian megathrust and up to 50 m (164 ft) in the shallow sections of the megathrust. The maximum slip is imposed along regions of the megathrust that have the capability to generate the highest amplitude waves near the southern coast of the Kenai Peninsula.

## Hypothetical Tsunami Sources

In this section, we describe tsunamigenic Alaska–Aleutian megathrust earthquakes used for Seward (table 3). Our goal is to determine geologically plausible scenarios that will result in maximum reasonable tsunami inundation in Seward and in northern Resurrection Bay—"credible worst-case scenarios." Scenarios 1–6 are based on results of the sensitivity study, geodetic data, and new thoughts regarding local megathrust behavior. Previously, the coseismic slip was limited to 18.5 m (60.7 ft) near the trench (fig. 6 in Suleimani and

others, 2005). Now, following modeling results for the USGS SAFRR project and considering implications of the 2011 Tohoku earthquake (Wang and others, 2018), we suggest that the maximum slip near the trench could be up to 50 m (164 ft). To be consistent with previous reports (e.g., Nicolsky and others, 2016, 2017; Suleimani and others, 2016), we consider four events (scenarios 7–10) with slip parameterization like that proposed by Butler and

others (2014). Scenario 11 models a rupture of the Cascadia subduction zone as an example of a distant tsunami source.

In all scenarios, we do not account for the finite speed of rupture propagation along the fault, and we consider the ocean-bottom displacements to be instantaneous. All proposed scenarios are summarized in table 3. The proposed slip distributions and vertical coseismic deformations are shown
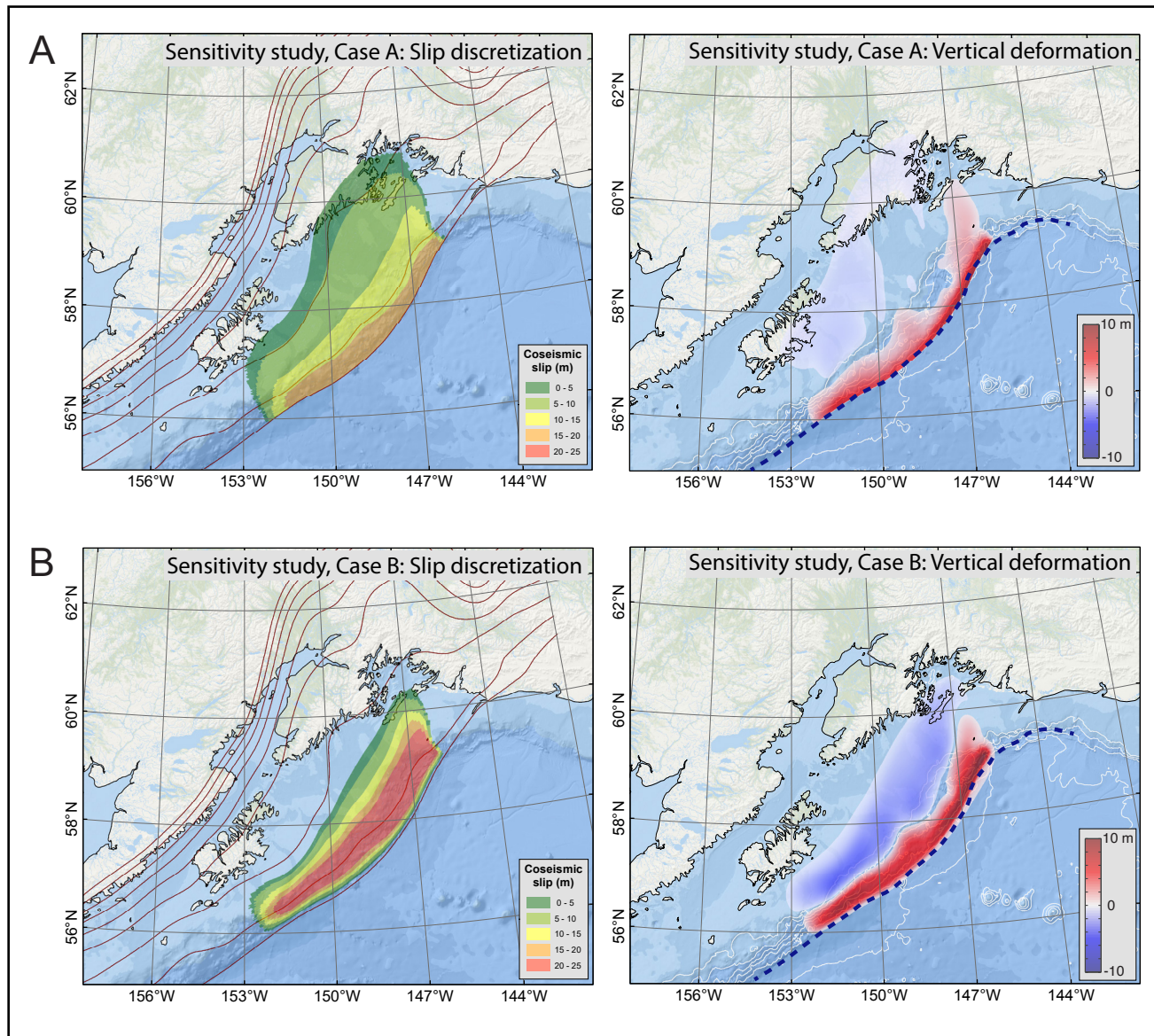


**Figure 5.** Imposed slip distribution along the plate interface (left), and computed vertical ground surface deformation (right) for sensitivity study cases A–D, modeling $M_w$ 9.0 ruptures near the Kenai Peninsula. The slip location varies in the downdip direction of the plate interface while preserving the same slip patch configuration. Red lines in the left images are depth contours of the subduction interface from 0–80 km with a 10-km interval. White lines in the right images are bathymetry contours within the depth range 1–5 km with a 1-km interval and the dashed blue line is the location of the seafloor trench.

in figure 7. We consider various downdip locations for the maximum slip to parameterize various credible tsunamigenic earthquakes. In the downdip direction, the slip is determined by the slip skewness parameter q in the Freund and Barnett (1976) formulae, and the along-strike slip distribution is uniform. For each scenario, the maximum slip is assumed to be located at a different depth range. We note that the presented scenarios are intended to capture the maximum credible scenarios and to provide a starting point for development of more complex models.
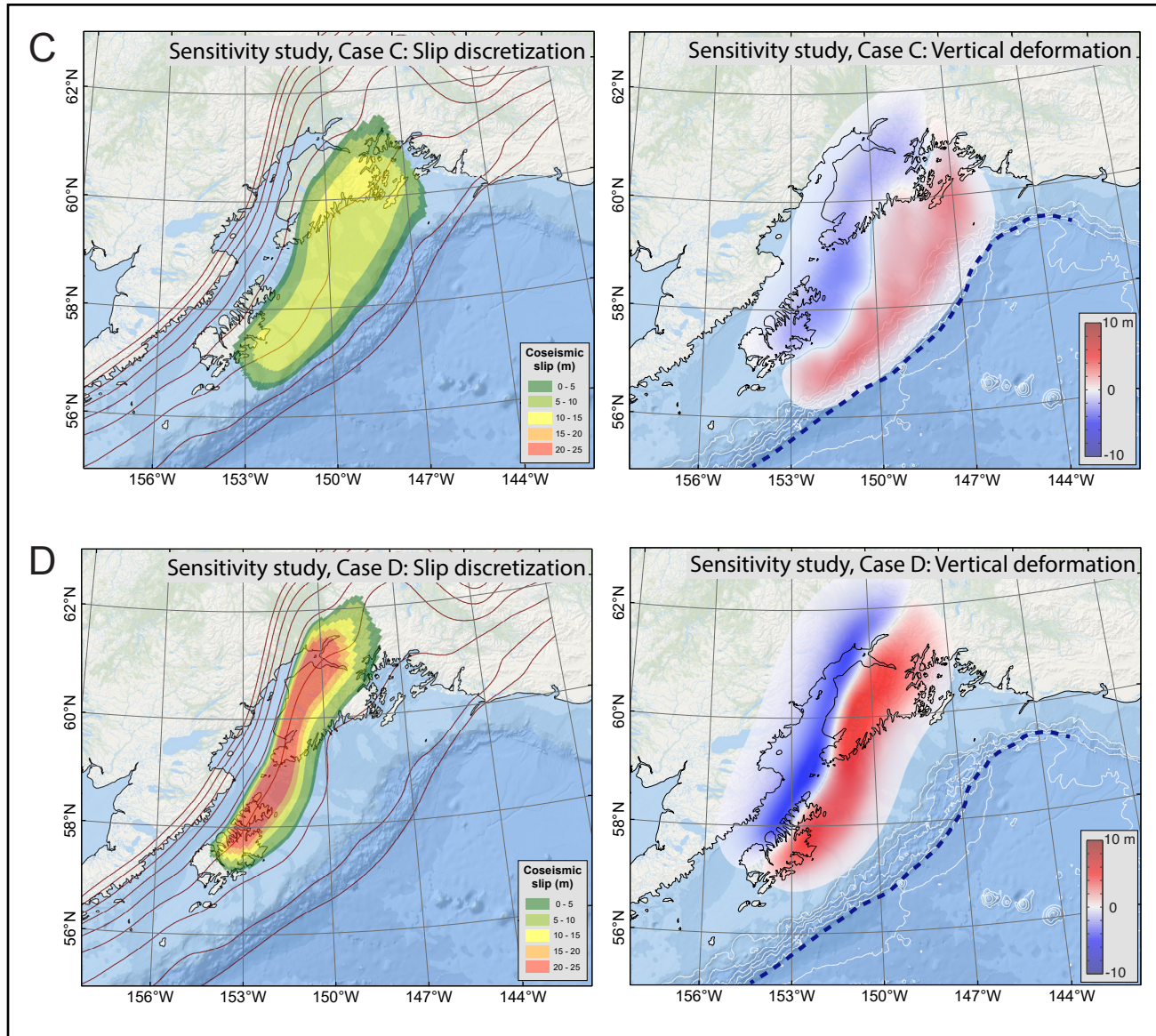


**Figure 5, continued.** Imposed slip distribution along the plate interface (left), and computed vertical ground surface deformation (right) for sensitivity study cases A–D, modeling $M_W$ 9.0 ruptures near the Kenai Peninsula. The slip location varies in the downdip direction of the plate interface while preserving the same slip patch configuration. Red lines in the left images are depth contours of the subduction interface from 0–80 km with a 10-km interval. White lines in the right images are bathymetry contours within the depth range 1–5 km with a 1-km interval and the dashed blue line is the location of the seafloor trench.
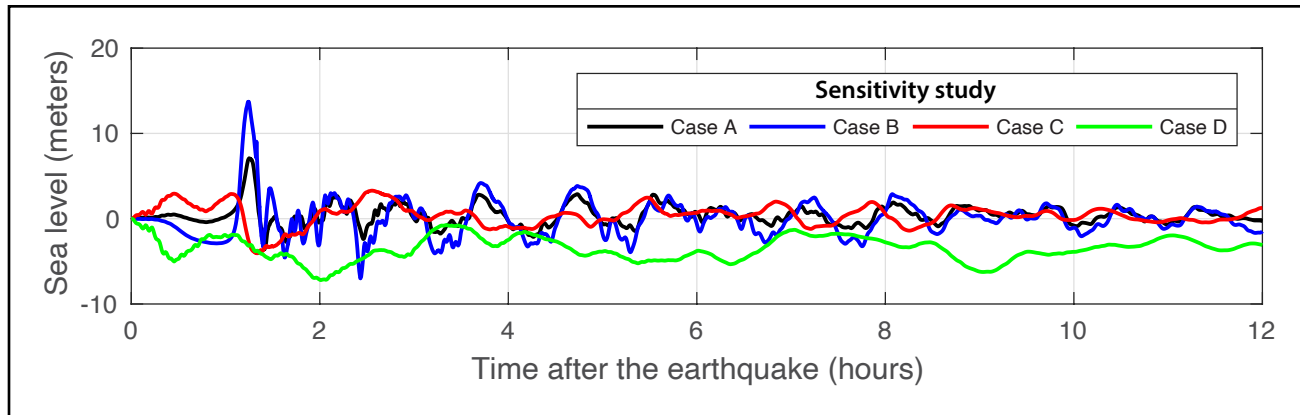
**Figure 6.** Modeled water-level dynamics (from the point of view of an observer standing at the shore) at Seward for the ground surface deformations shown in figure 5. Model duration is 12 hours.

**Table 3.** Hypothetical megathrust scenarios in the Gulf of Alaska between Prince William Sound and Kodiak Island (except for scenario 11), used to model tsunami runup in Seward. Asterisk indicates scenarios that have been considered in previous inundation mapping reports.

| Megathrust scenario number | Description | Depth range km (mi) | Maximum slip depth range km (mi) | Maximum slip m (ft) | Maximum subsidence m (ft) | Maximum uplift m (ft) |
|---|---|---|---|---|---|---|
| 1 | $M_W$ 9.2 earthquake; 10 km depth | 0-25 (0-15.5) | 5-15 (3.1-9.3) | 35.0 (115.0) | 5.6 (18.3) | 14.0 (45.9) |
| 2 | $M_W$ 9.25 earthquake; 20 km depth | 10-30 (6.2-18.6) | 15-25 (9.3-15.5) | 35.0 (115.0) | 6.4 (20.9) | 8.0 (26.2) |
| 3 | $M_W$ 9.0 earthquake; 30 km depth | 20-40 (12.4-24.8) | 27-33 (16.8-20.5) | 35.0 (115.0) | 6.7 (21.9) | 7.3 (23.9) |
| 4 | $M_W$ 9.3 earthquake; 20-30 km depth | 10-40 (6.2-24.8) | 20-30 (12.4-18.6) | 35.0 (115.0) | 7.3 (23.9) | 6.0 (19.7) |
| 5 | $M_W$ 9.3 earthquake; 15-20 km depth | 10-40 (6.2-24.8) | 15–20 (9.3-12.4) | 35.0 (115.0) | 4.9 (16.0) | 10.8 (35.4) |
| 6 | $M_W$ 9.25 earthquake; 25-30 km depth | 10-40 (6.2-24.8) | 25-35 (15.5-21.7) | 50 (164.0) | 7.6 (24.9) | 5.3 (17.4) |
| 7* | $M_W$ 9.3 earthquake with 35 m of maximum slip across most of the rupture | 2–38 (1.2–23.6) | 5–22 (3.1-13.7) | 35.0 (115.0) | 8.0 (26.2) | 13.7 (44.9) |
| 8* | $M_W$ 9.3 earthquake with 50 m of maximum slip close to the trench | 2–38 (1.2–23.6) | 5-12 (3.1-7.4) | 50 (164.0) | 2.7 (8.8) | 20.0 (65.6) |
| 9 | $M_W$ 9.25 earthquake; 10 km depth, slip extending to 0 km depth | 0-25 (0-15.5) | 0-12 (0-7.4) | 35.0 (115.0) | 2.7 (8.8) | 19.2 (62.9) |
| 10* | $M_W$ 9.0 earthquake with 50 m of maximum slip in the shallow part of the rupture | 0–31 (0-19.2) | 0–18 (0-11.2) | 50 (164.0) | 8.4 (27.5) | 30.8 (101.0) |
| 11* | $M_W$ 9.1 earthquake in the Cascadia subduction zone | 45.0 (150.0) | 36.0 (120.0) | 45.0 (148.0) | 8.0 (25.0) | 11.0 (35.0) |

**Blind Rupture Scenarios**

These scenarios simulate hypothetical ruptures at the eastern end of the Alaska–Aleutian megathrust where the updip and downdip limits of the rupture are 0 km and 40 km (24.8 mi), respectively. The proposed slip distributions and vertical coseismic deformations for scenarios 1–6 are shown in figure 7A–F.

| | |
|---|---|
| **Scenario 1: M$_W$ 9.2 earthquake; 10 km (6.2 mi) depth** | The depth of maximum slip corresponds to the depth for sensitivity case B. The slip skewness parameter, q, is set to 0.2 (bell-shaped curve skewed toward the shallow part of the rupture) to model the maximum slip of 35 m (115 ft) at a depth of 10 km (6.2 mi). |
| **Scenario 2: M$_W$ 9.25 earthquake; 20 km (12.4 mi) depth** | The depth of maximum slip corresponds to the depth for sensitivity case C. The slip skewness parameter, q, is set to 0.5 (bell-shaped curve is not skewed) to model the maximum slip of 35 m (115 ft) at a depth of 20 km (12.4 mi). |
| **Scenario 3: M$_W$ 9.0 earthquake; 30 km (18.6 mi) depth** | The depth of maximum slip corresponds to the depth for sensitivity case D. The slip skewness parameter, q, is set to 0.5 (bell-shaped curve is not skewed) to model the maximum slip of 35 m (115 ft) at a depth of 30 km (18.6 mi). |
| **Scenario 4: M$_W$ 9.3 earthquake; 20–30 km (12.4–18.6 mi) depth** | The depth of maximum slip corresponds to that for the combination of sensitivity cases C and D. The slip skewness parameter, q, is set to 0.5 (bell-shaped curve is not skewed) to model the maximum slip of 35 m (115 ft) distributed between the depths of 20 km (12.4 mi) and 30 km (18.6 mi). |
| **Scenario 5: M$_W$ 9.3 earthquake; 15–20 km (9.3–12.4 mi) depth** | The depth of maximum slip corresponds to the depth for sensitivity case B. The slip skewness parameter, q, is set to 0.2 (bell-shaped curve skewed toward the shallow part of the rupture) to model the maximum slip of 35 m (115 ft) distributed between the depths of 15 km (9.3 mi) and 20 km (12.4 mi). |
| **Scenario 6: M$_W$ 9.25 earthquake; 25–30 km (15.5–18.6 mi) depth** | The depth of maximum slip corresponds to the depth for sensitivity case D. The slip skewness parameter, q, is set to 0.7 (bell-shaped curve skewed toward the deeper part of the rupture) to model the maximum slip of 35 m (115 ft) at a depth of 30 km (18.6 mi). |

## Surface-Breaching Rupture Scenarios

Ryan and others (2012), and later Kirby and others (2013), compared the Alaska and Tohoku margins and suggested that a hypothetical rupture in the Alaska–Aleutian subduction zone might propagate to shallow depths as it did in the $M_W$ 9.0 Tohoku earthquake. Shallow fault rupture at the Tohoku margin resulted in a complex mix of blind (concealed) fault-bend folding along the fault length and surface-breaching rupture of the seafloor—both of which contributed to significant seafloor disturbance. Multibeam bathymetry in the eastern part of the Aleutian megathrust suggests that the Alaska plate margin has similar mixed-behavior shallow ruptures.

Recently Butler and others (2014) described a layer of sand discovered in the Makauwahi sinkhole on the island of Kaua'i, Hawai'i. The origin of this layer was presumed to be inundation of the sinkhole by a giant paleotsunami following a $M_W$ 9+ earth-quake in the eastern Aleutian Islands. Butler (2012) provides an in-depth examination of previous great Aleutian earthquakes and tsunamis impacting Hawai'i. In subsequent research Butler (2014) considered several hypothetical events with a 35 m (114.8 ft) displacement on the megathrust and up to a 50 m (164 ft) displacement near the trench.

Scenarios 7–10 simulate various hypothetical ruptures in the eastern part of the Alaska–Aleutian megathrust where the updip and downdip limits of the rupture are between 0 km and 30–40 km (18.6–24.8 mi), respectively. However, we account for the possibility that the slip in the earthquake rupture may be concentrated at the shallowest depths of the plate interface and may breach the sea floor at the trench. We construct scenarios 7–10 with modeled fault slip extending to the shallowest part of the megathrust. The proposed slip distributions and vertical coseismic deformations for scenarios 7–10 are shown in figure 7G–J.

| | |
|---|---|
| **Scenario 7: $M_W$ 9.3 earthquake with 35 m (114.8 ft) of maximum slip in most of the rupture** | In this scenario, like Butler (2014), we assume 35 m (114.8 ft) of slip for nearly the entire rupture patch between the 5 km (3.1 mi) and 35 km (21.7 mi) depth contours, with slip decreasing both toward the trench and to the deeper parts of the rupture. A similar scenario was proposed in the tsunami modeling study for Kodiak (scenario 8 of Suleimani and others, 2017). |
| **Scenario 8: $M_W$ 9.3 earthquake with 50 m (164 ft) of maximum slip close to the trench** | The depth of maximum slip corresponds to the depth for sensitivity case B. The slip skewness parameter, q, is set to 0.25 (bell-shaped curve skewed toward the trench) to model the maximum slip of 50 m (115 ft) at a depth of 10 km (6.2 mi), and then slip gradually reduces to about 10 m (33 ft) at 30 km (18.6 mi) depth. This scenario was used in previous tsunami inundation mapping reports (for example, Suleimani and others, 2013, 2016; Nicolsky and others, 2017, 2018). |
| **Scenario 9: $M_W$ 9.25 earthquake; 10 km (6.2 mi) depth, slip extending to 0 km depth** | The depth of maximum slip corresponds to the depth for sensitivity case A. The slip skewness parameter, q, is set to 0.2 (bell-shaped curve skewed toward the trench) to model the maximum slip of 35 m (115 ft) between depths of 0 and 15 km (9.3 mi), and then slip gradually reduces to about 10 m (33 ft) at 25 km (15.5 mi) depth. |

| Scenario 10: M<sub>W</sub> 9.0 earthquake with 50 m (164 ft) of maximum slip in the shallow part of the rupture | In this scenario, like Butler (2014), we assume 20 m (65.6 ft) slip on the plate interface between the 17.9 km (11.1 mi) and 30.8 km (19.1 mi) depth contours, and up to 50 m (164 ft) slip near the trench between 0 km (0 mi) and 17.9 km (11.1 mi) depth. A similar scenario was proposed in the tsunami modeling study for Kodiak (scenario 9 of Suleimani and others, 2017). |
|---|---|
| Scenario 11: Rupture of the Cascadia subduction zone, including the entire megathrust between British Columbia and northern California | Scenario 11 considers a hypothetical tsunami generated along the coast of the Pacific Northwest U.S.—relatively distant from the Kenai Peninsula. Although a rupture of the Cascadia subduction zone is not a worst-case scenario Seward, this scenario is included for the sake of community preparedness. This scenario is the same as Scenario 16 in the tsunami modeling studies for King Cove and Cold Bay (Suleimani and others, 2016). The slip distribution model for this scenario is shown in figure 10 of Wang and others (2003). The vertical coseismic deformations for scenario 11 are shown in figure 7K. |

## TSUNAMI SOURCES WITH SPLAY FAULTS

Splay faults are potentially important secondary tsunami sources in megathrust earthquakes. These steeply dipping faults that branch from the subduction zone to the seafloor can produce large coseismic deformations that significantly increase tsunami runup heights in the near field (figs. 8 and 9; e.g., Lotto and others, 2019; Wang and Tréhu, 2016; Heidarzadeh, 2011). Also, because the splay faults intersect the seafloor landward of the seafloor trench, tsunami waves produced by slip on a splay fault will arrive before the waves generated by slip on the megathrust; thus, if slip on a splay fault is significant the initial tsunami wave can arrive sooner, reducing available time for evacuation.

Several studies published in the years following the 1964 Great Alaska Earthquake analyzed data on coseismic displacements and land features associated with offshore splay faults, as well as tsunami arrival times and tsunami amplitudes along the coast of the Kenai Peninsula and Kodiak Island (Plafker, 1965, 1967, 1969; Plafker and others, 1969). Plafker (1965) showed that slip during great megathrust earthquakes can be partitioned between the subducting boundary and splay faults. He demonstrated that the slip distribution in the 1964 rupture included a substantial amount of slip on intraplate splay faults, resulting in up to 10 meters of surface offset on the Patton Bay fault (fig. 1). Plafker suggested that the Patton Bay fault marks the northern end of a system of discontinuous faults in the ocean floor that continues well past where it was mapped at that time. More recently, Liberty and others (2013) analyzed high-resolution seismic reflection data for the PWS area of the 1964 rupture and found that the greatest coseismic uplift in that region occurred on a series of splay faults. The authors examined the fault offsets on splay faults west of Montague Island (fig. 1) and found that several splay faults had accumulated significant slip over the Holocene. Liberty and others (2019) showed that repeated ruptures of a set of splay faults with a slip pattern like that seen in 1964 had occurred along with past megathrust earthquakes. They concluded that the extent of rupture on the splay faults was linked to the along-strike limits of the PWS asperity (fig. 1), and that the asperity had been persistent over many earthquake cycles.

Savage and others (2014) analyzed GPS surveys (1993–2012) on Middleton Island, located

**Figure 7.** Estimated slip distribution along the plate interface and computed vertical ground surface deformation for (**A, B, C**) scenarios 1–3. Red lines are depth contours of the subduction interface within the depth range 0-80 km with a 10-km interval. White lines are bathymetry contours within the depth range 1–5 km with a 1-km interval and dashed blue line is the location of the seafloor trench.
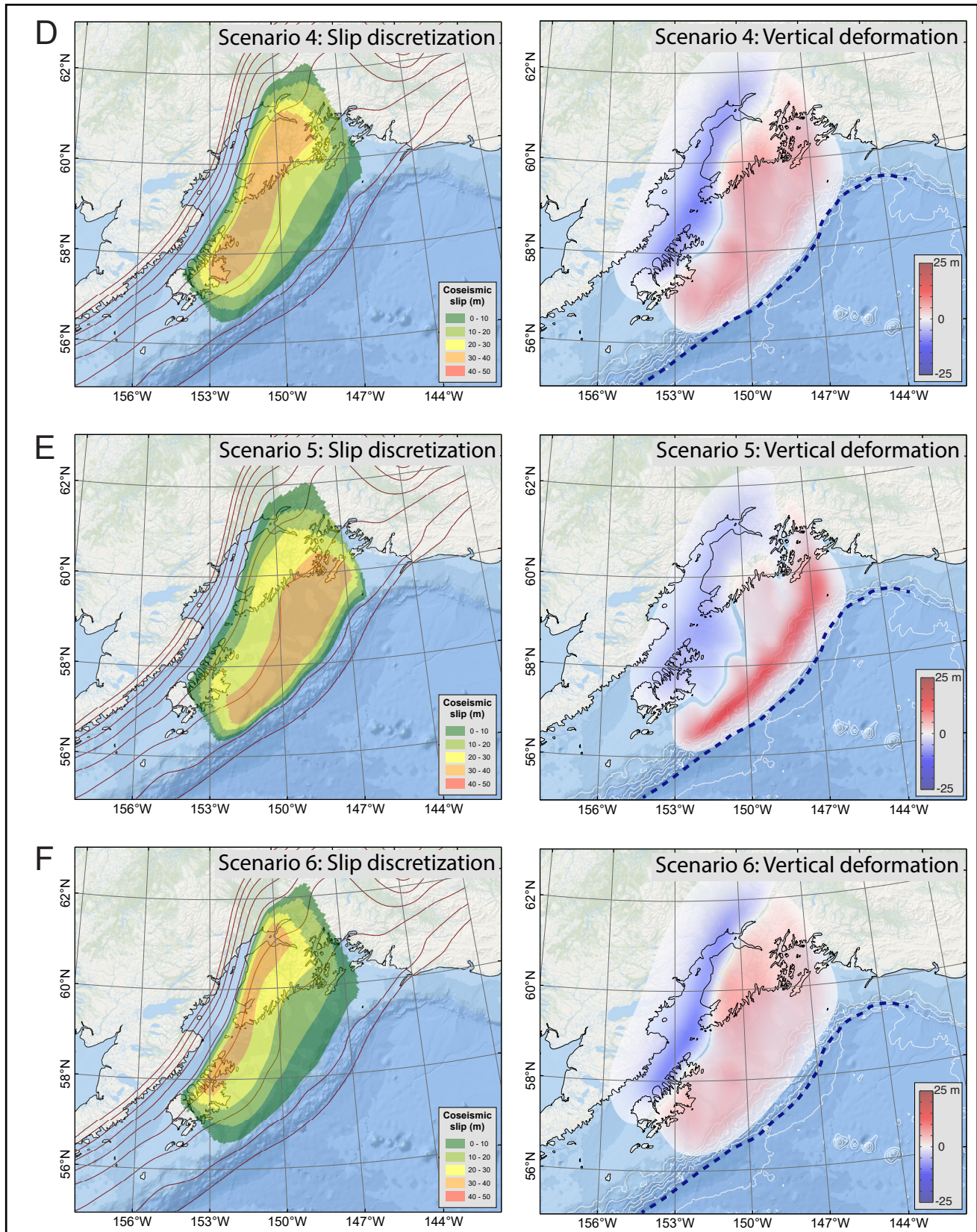
**Figure 7, continued.** Estimated slip distribution along the plate interface and computed vertical ground surface deformation for (**D, E, F**) scenarios 4–6. Red lines are depth contours of the subduction interface within the depth range 0-80 km with a 10-km interval. White lines are bathymetry contours within the depth range 1–5 km with a 1-km interval and dashed blue line is the location of the seafloor trench.
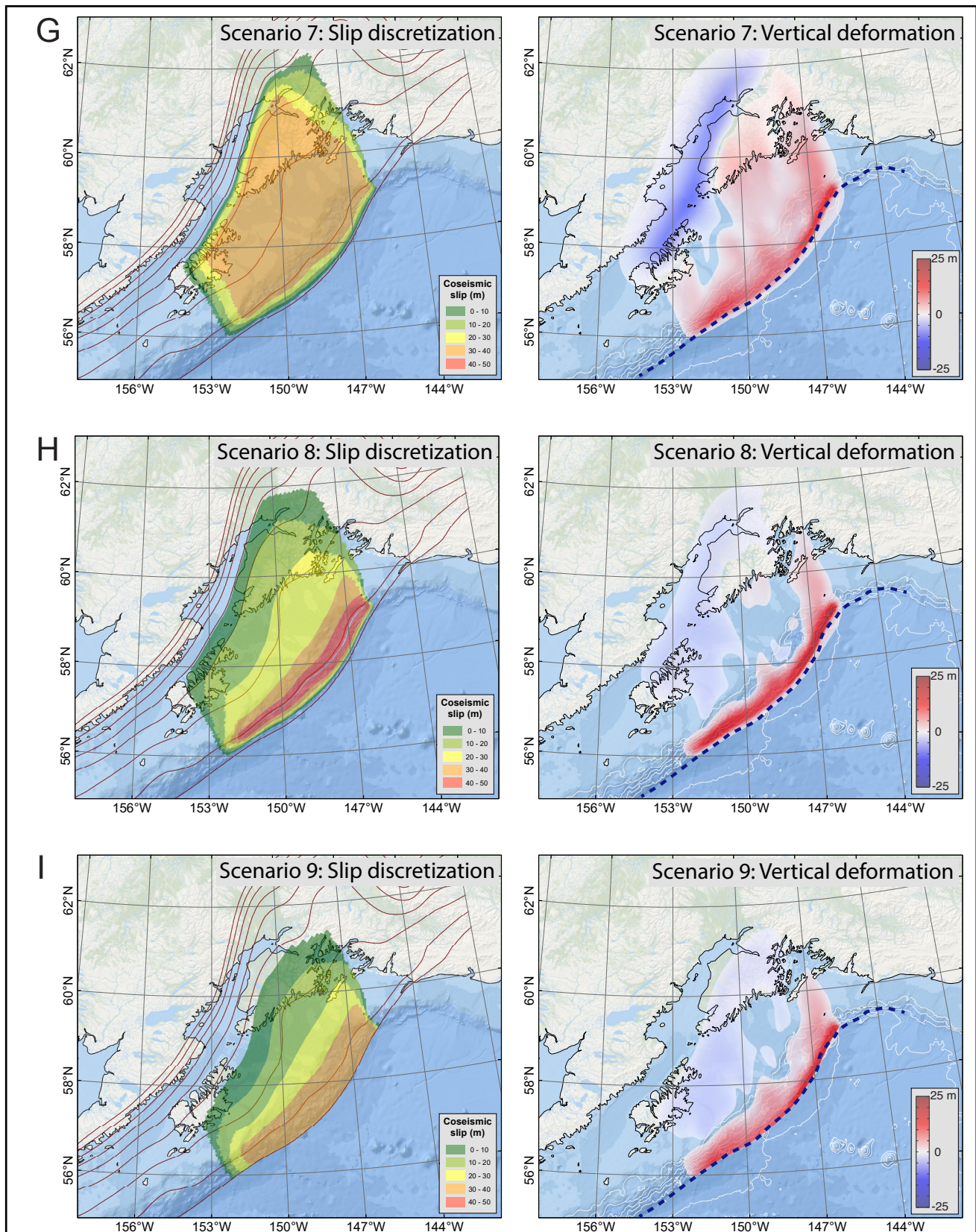
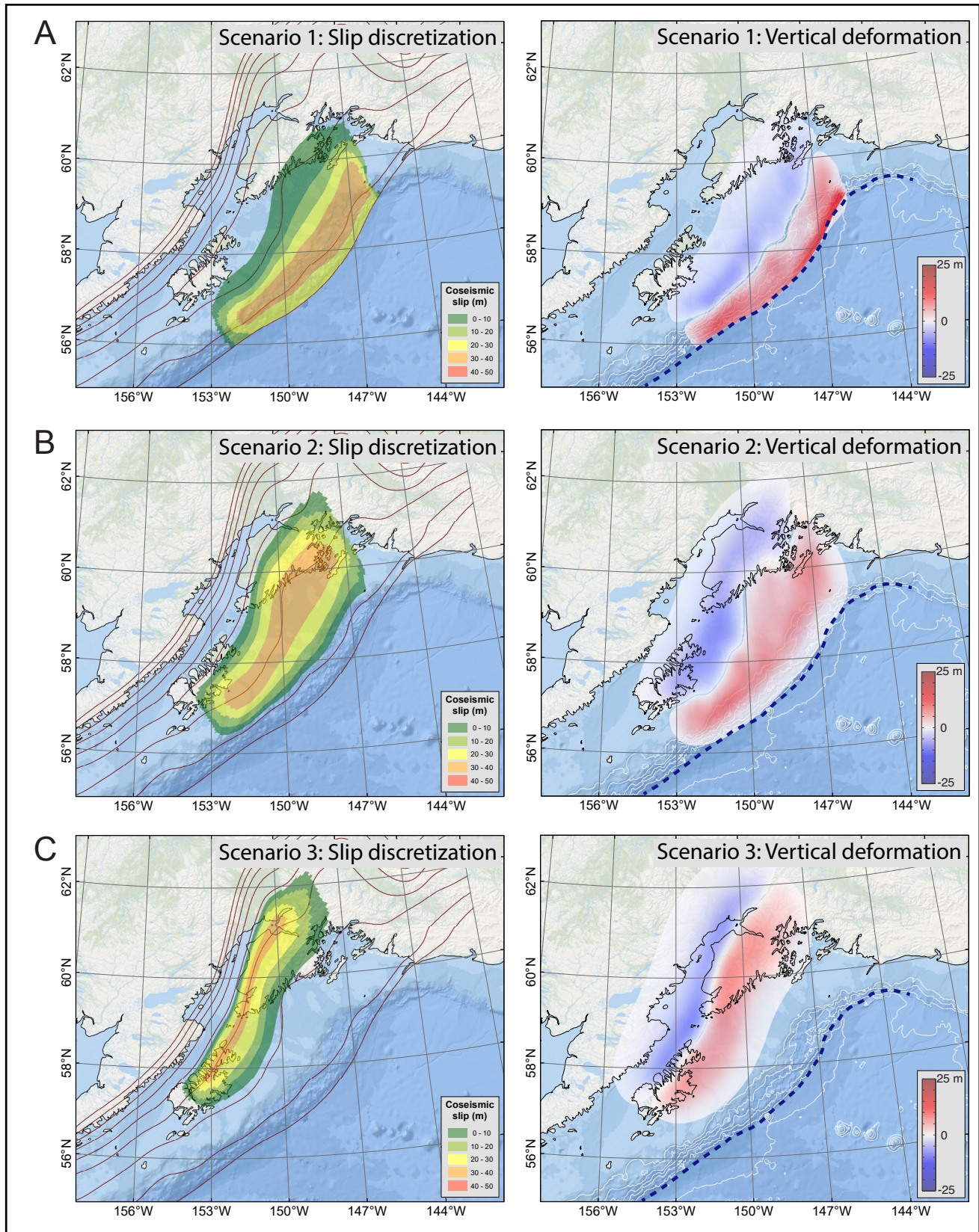**Figure 7, continued.** Estimated slip distribution along the plate interface and computed vertical ground surface deformation for (**G, H, I**) scenarios 7–9. Red lines are depth contours of the subduction interface within the depth range 0-80 km with a 10-km interval. White lines are bathymetry contours within the depth range 1–5 km with a 1-km interval and dashed blue line is the location of the seafloor trench.
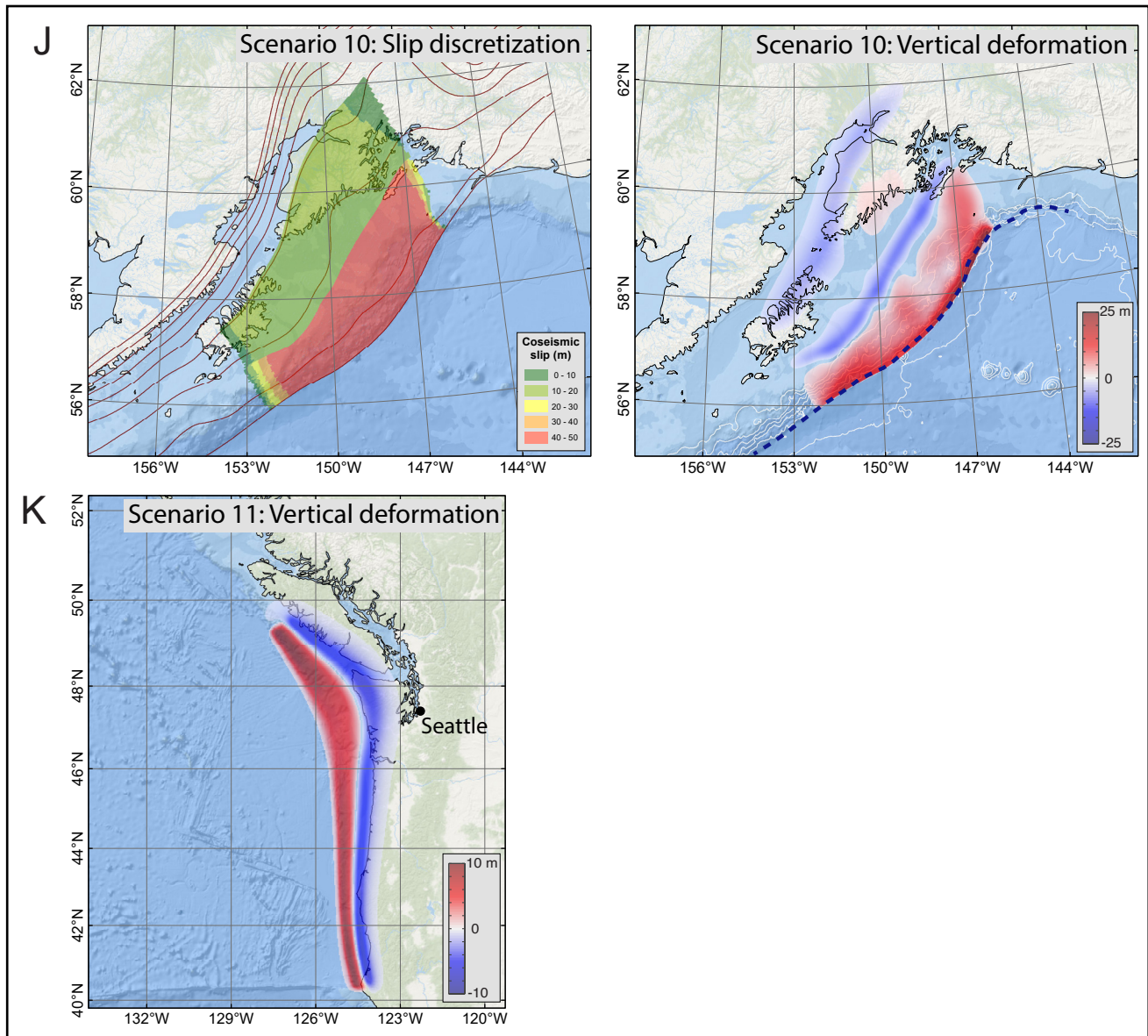
**Figure 7, continued.** Estimated slip distribution along the plate interface for (**J, K**) scenarios 10 and 11 and computed vertical ground surface deformation for scenario 11 (slip distribution is not provided for scenario 11). Red lines are depth contours of the subduction interface within the depth range 0–80 km with a 10-km interval. White lines are bathymetry contours within the depth range 1–5 km with a 1-km interval and dashed blue line is the location of the seafloor trench.

only 50 km from the base of the inner wall of the Aleutian Trench (fig. 1). Measurements indicate that the island is currently being uplifted at a rate of about 14 mm/yr (0.6 in/yr). The authors conclude that the apparent cause of the uplift is continuous slip on a splay fault branching off from the megathrust landward of Middleton Island but outcropping seaward of the island, and that the very existence of Middleton Island so close to the trench suggests the existence of a splay fault there.

Using seismic reflection imagery, legacy seismic data, and high-resolution bathymetry, von Huene and others (2021) identified Aleutian trench backstops, which are splay fault zones that separate the accretionary prism from the continental margin and are the boundaries along which weak sediment accreted. The authors suggest that the backstop splay fault zones extend along the entire Aleutian arc and contribute to regional tsunami hazards. From the analysis of slip distribution and coseismic

displacements in the 1964 Great Alaska Earthquake, the authors proposed that the backstop splay faults in the KI asperity (fig. 1) possibly contributed to generation of the 1964 tsunami. Since the slip partitioning between the splay fault and megathrust is not well understood due to lack of direct seafloor measurements during earthquakes (Heidarzadeh, 2011; Li and others, 2014), one cannot rule out the possibility of slip along the backstop splay faulting zone offshore of the Kenai Peninsula in the next megathrust earthquake.

To avoid understating hazards, a tsunami hazard assessment must consider the effect of possible splay fault branching during a large subduction zone earthquake (Heidarzadeh, 2011; Wang and Tréhu, 2016). In this report we consider several tsunami scenarios with added splay faults and study their effects on tsunami waves at Seward and in northern Resurrec-

tion Bay. Figure 8 shows the shelf area in the Gulf of Alaska between the lower Cook Inlet and the Aleutian trench. We assume that slip can be partitioned between the megathrust and a splay fault offshore of the Kenai Peninsula in one of the following three areas: PBIE1 and PBIE2, the inferred extensions of the Patton Bay splay fault system that connect to the landward and trenchward boundaries of the Kodiak shelf fault zone, respectively, and the backstop (BS) splay fault zone described by von Huene and others (2021). The three solid lines between the island and trench—which go through these fault zones—are surface traces of the proposed splay faults (fig. 8). There are no direct constraints on the potential along-strike rupture extent of the splay faults in this area, but partially concealed faults are present along the entire length of the study area (fig. 8), so we assume the splay faults to be long enough to produce a wave
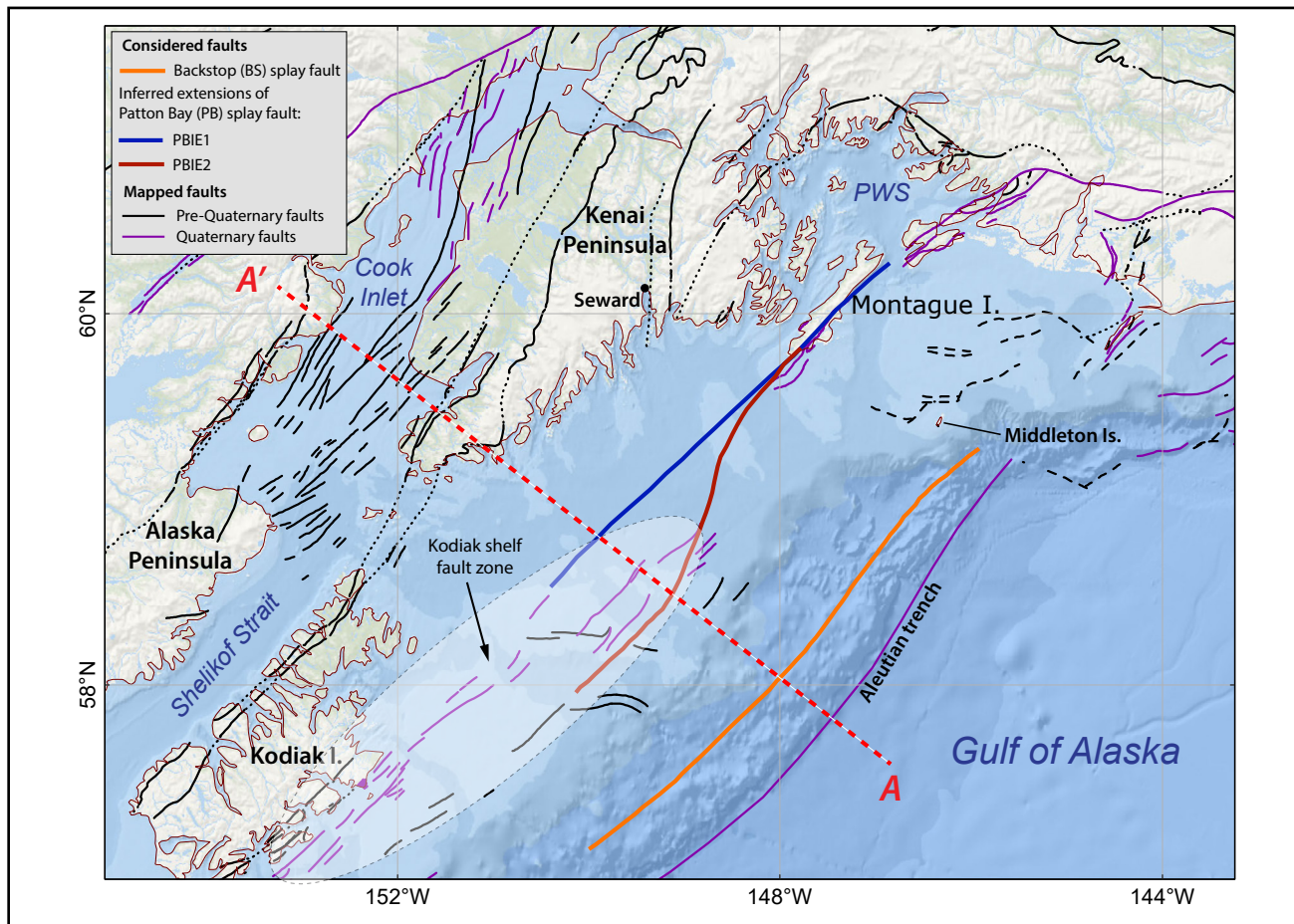


**Figure 8.** Shelf area in the Gulf of Alaska between the southern coast of the Kenai Peninsula and the Aleutian trench, with locations of the inferred extensions of the Patton Bay fault (PBIE1 and PBIE2) and the backstop (BS) splay fault. The A-A' profile (red dashed line) across the Aleutian megathrust is shown in figure 9.

front that can influence tsunami runup in Resurrection Bay. The A-A' cross-sectional profile across the Alaska–Aleutian megathrust (fig. 9) illustrates the splay faults rising from the megathrust. We develop splay fault scenarios based on these three possible locations of splay fault branching (fig. 10). For the extensions of the Patton Bay fault, we make two splay fault scenarios, PBIE1 and PBIE2, with dips of 60° and 45°, respectively. The splay fault dips decrease with depth until the splay fault intersection with the plate interface. For the BS location, we select 30° dip at the surface, based on the values between 21° and 39° derived from seismic imagery for the eastern part of the Alaska–Aleutian megathrust (von Huene and others, 2021). The resultant splay fault geometry was checked to ensure that it is tightly connected to the plate interface, and then was discretized (similarly to the plate interface) into many rectangular subfaults.

The goal of adding a splay fault to a megathrust earthquake is to create a scenario that accounts for potential increases in tsunami height due to more complex earthquake ruptures. Another effect of a splay fault is a shorter wave arrival time, an important factor considered by emergency managers during evacuation planning, as well as by pedestrian evacuation modeling tools. Therefore, we construct the splay fault scenarios based on the following considerations:

**Distance from the coast.** To determine how the distance from the coast affects wave height, we consider three different locations of the splay fault surface traces with respect to the coast of the Kenai Peninsula: the PBIE1, PBIE2, and BS zones (fig. 8).

**Selection of the megathrust scenarios.** We have chosen to augment three megathrust scenarios by adding a splay fault. The selected scenarios are those which result in the largest tsunami inundation areas (see Modeling Results section; several scenarios can produce a similar extent of inundation), and satisfy one of the following conditions: either the scenario has the maximum amount of slip in the area of the rupture where the splay fault connects to the megathrust, or the scenario results in the maximum amount of ground subsidence in the community. Scenarios 2, 4, 6, 7, and 8 (table 3) fit these criteria.

**Slip partitioning.** Because the pattern of slip partitioning between the megathrust and splay faults is poorly understood (Wendt and others, 2009), we consider different ways to divide the slip in combined megathrust/splay fault ruptures by reducing the slip on the megathrust updip of the splay fault by either 20 or 50 percent.

To build a set of combined megathrust/splay fault ruptures, we add each of the splay fault
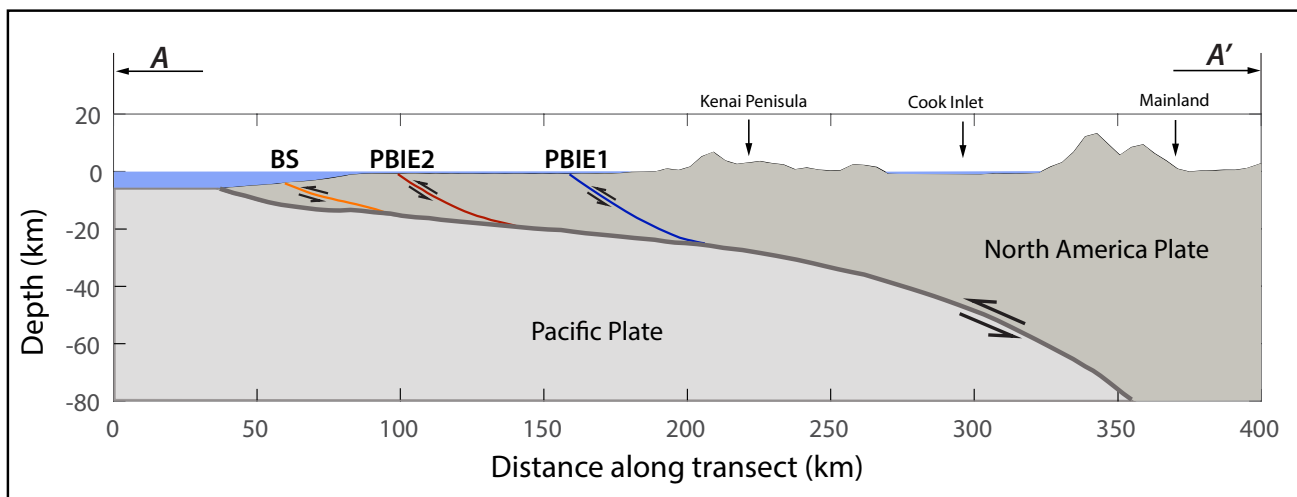


**Figure 9.** The A-A' profile across the Aleutian megathrust. The elevation values are exaggerated by a factor of 10 to illustrate the topography of the Kenai and Alaska peninsulas.
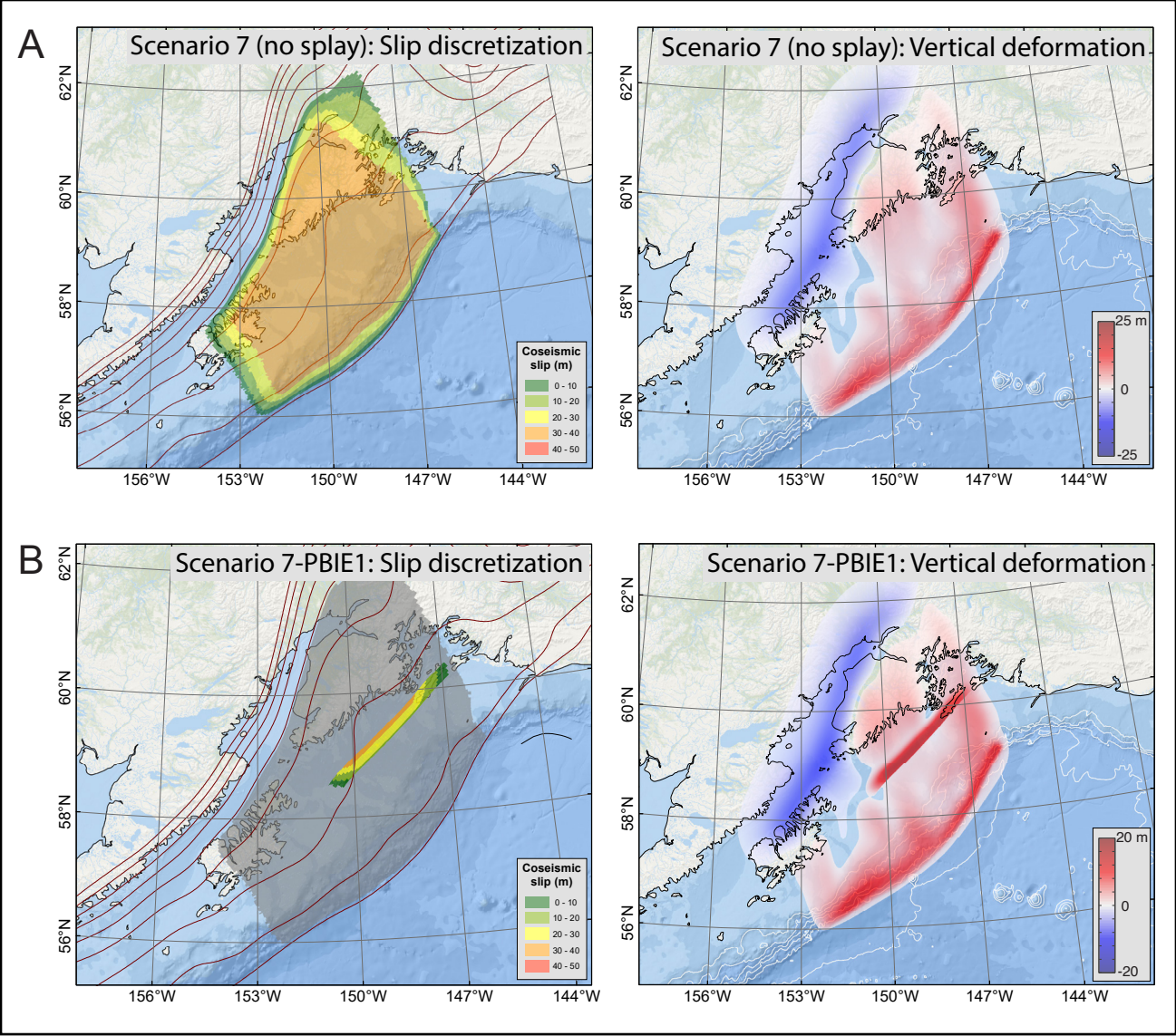
**Figure 10.** Assumed slip distribution along the plate interface (left), and computed vertical ground surface deformation (right) for (**A**) the megathrust-only scenario 7 and (**B**) scenario 7 with an added splay fault PBIE1.

ruptures outlined in table 4 to megathrust scenarios 2, 4, 6, 7, and 8. We choose these scenarios because: A) inclusion of splay fault ruptures reduces first wave arrival times (i.e., the surface trace of the splay fault is closer to Seward than is the area of maximum seafloor uplift due to slip on the megathrust); and B) plausible splay faults (inferred surface traces combined with appropriate dips) root into the megathrust where there is sufficient slip for the splay fault to rupture to the seafloor. Figure 10 illustrates

**Table 4.** Splay fault scenarios.

| Description | Scenario name | Dip (degrees) |
|---|---|---|
| Patton Bay fault system Inferred Extension 1 | PBIE1 | 60 |
| Patton Bay fault system Inferred Extension 2 | PBIE2 | 45 |
| Backstop fault system | BS | 30 |
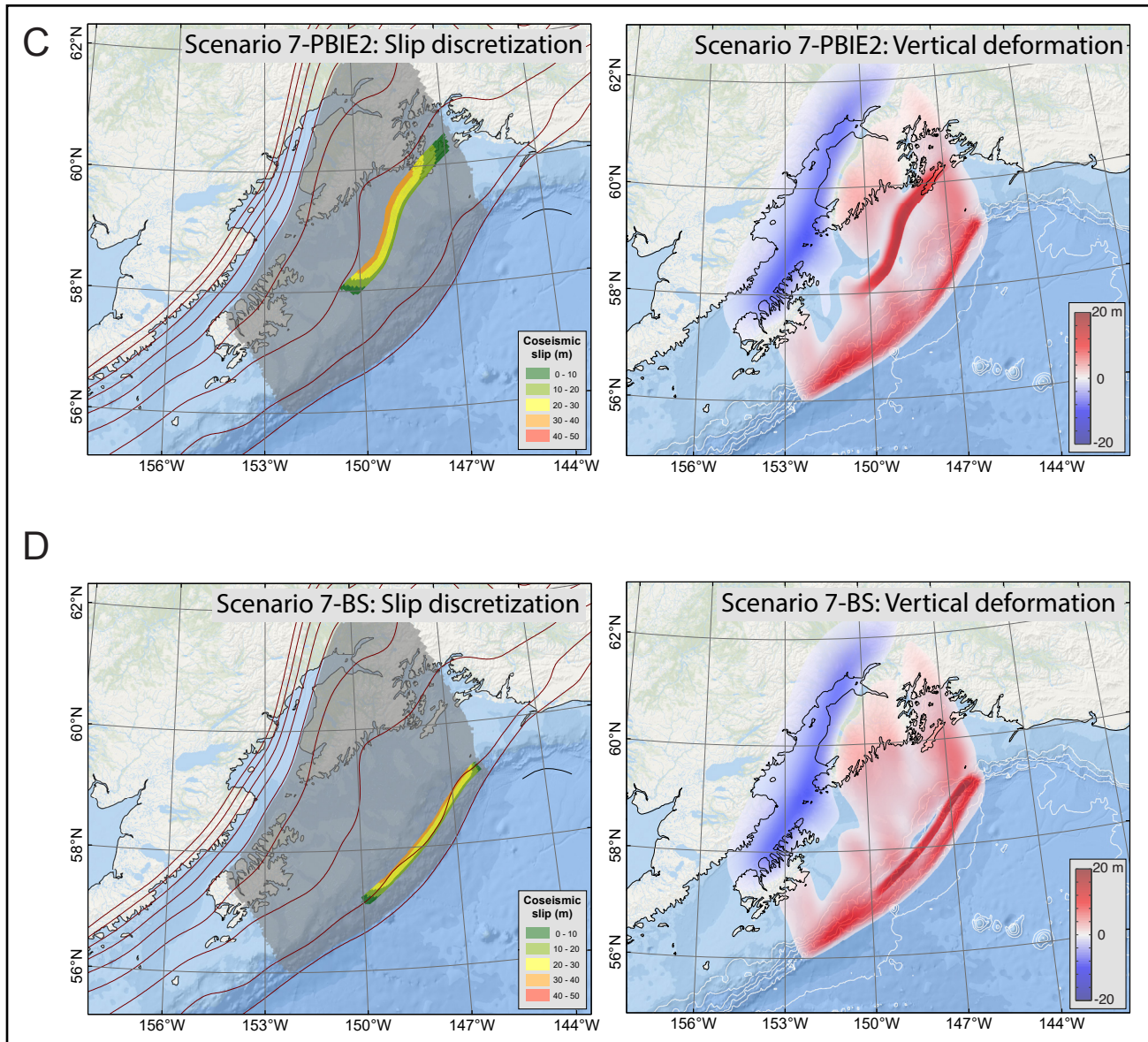
**Figure 10, continued.** Assumed slip distribution along the plate interface (left), and computed vertical ground surface deformation (right) for (**C**) scenario 7 with an added splay fault PBIE2 and (**D**) scenario 7 with an added splay fault in the BS zone.

this process using the example of scenario 7. The proposed slip distributions and vertical coseismic deformations are shown in the left and right columns, respectively. Figure 10A shows scenario 7 without the splay fault for reference. Figures 10B–D show the splay fault slip patterns and the combined coseismic deformations for PBIE1, PBIE2, and BS splay faults. Note the difference in vertical deformation scale bar between the original scenario 7 (fig. 10A) and the new scenarios that include a splay fault (fig. 10B–D). The left columns in figures 10B–D are

the slip patterns for splay faults shown on top of the megathrust rupture area to illustrate the proximity of splay faults to Seward. The coseismic deformations in the right column illustrate that for the cases of PBIE1 and PBIE2 splay faults, there is an area of second maximum uplift that is much closer to the coast than the maximum in the trench area.

The full list of scenarios and splay fault parameters is given in table 5. The first column shows scenario numbers for megathrust-only scenarios

**Table 5.** All hypothetical megathrust and splay fault scenarios used to model tsunami runup in upper Resurrection Bay and Seward.

| Mega-thrust scenario number (from table 3) | Splay fault scenario number | Description | Dip | Maximum slip on splay fault, m (ft) | Slip reduction on the plate interface updip of the splay fault |
|---|---|---|---|---|---|
| 1 | | $M_W$ 9.2 earthquake; 10 km depth | | | |
| 2 | | $M_W$ 9.25 earthquake; 20 km depth | | | |
| | 2-PBIE1 | Megathrust scenario 2 with the added splay fault as an inferred extension 1 of the Patton Bay fault | 60° | 37.7 (123.7) | 20% |
| 3 | | $M_W$ 9.0 earthquake; 30 km depth | | | |
| 4 | | $M_W$ 9.3 earthquake; 20-30 km depth | | | |
| | 4-PBIE1 | Megathrust scenario 4 with the added splay fault as an inferred extension 1 of the Patton Bay fault | 60° | 30.1 (98.7) | 50% |
| 5 | | $M_W$ 9.3 earthquake; 15-20 km depth | | | |
| 6 | | $M_W$ 9.25 earthquake; 25-30 km depth | | | |
| | 6-PBIE1 | Megathrust scenario 6 with the added splay fault as an inferred extension 1 of the Patton Bay fault | 60° | 19.7 (64.6) | 50% |
| 7 | | $M_W$ 9.3 earthquake with 35 m of maximum slip across most of the rupture | | | |
| | 7-PBIE1 | Megathrust scenario 7 with the added splay fault as an inferred extension 1 of the Patton Bay fault | 60° | 35.4 (116.1) | 20% |
| | 7-PBIE2 | Megathrust scenario 7 with the added splay fault as an inferred extension 2 of the Patton Bay fault | 45° | 35.1 (115.1) | 20% |
| | 7-BS | Megathrust scenario 7 with added splay fault in the backstop fault zone | 30° | 34.5 (113.2) | 20% |
| 8 | | $M_W$ 9.3 earthquake with 50 m of maximum slip close to the trench | | | |

given in table 3; and the second column refers to the splay fault scenario numbers.

## Time Series

The arrival time of the first wave, the maximum wave amplitude, and the duration of wave action are all important factors that should be considered by emergency managers during evacuation planning. Therefore, we supplement the inundation maps with time series of modeled water level and velocity dynamics at selected locations in Resurrection Bay and Seward. Appendix A contains plots of sea level and velocity time series for selected scenarios at critical locations. For each location—shown by a number in figure A1, we plot the sea level and water velocity (fig. A2) for selected scenarios (scenarios 1, 3, 5, 7, 9, 10, and 11). Scenarios 1, 3, and 5 represent the blind rupture group of scenarios, and scenarios

7, 9, and 10 are from the surface-breaching group of scenarios. Scenario 11 is included as an example of a potential far-field event.

In all plots in Appendix A, zero time corresponds to the time at which the earthquake occurs. The pre-earthquake elevation/depth with respect to the MHHW is stated for each location. The post-earthquake elevation/depth corresponding to the MHHW datum is also listed for each scenario in table A1. To show the height of arriving tsunamis for offshore locations, we use a vertical datum with a zero-mark corresponding to the pre-earthquake sea level. Velocity was computed only where the water depth is greater than 0.3 m (1.0 ft). The velocity magnitude is calculated as water flux divided by water depth, thus the uncertainty can be large when the water depth is small.

The maximum water level for all considered scenarios are listed in appendix table A2, and maximum velocity values are given in table A3.

## MODELING RESULTS

We modeled water dynamics for each of the scenarios that are described above and summarized in table 4. The extent of inundation and flow depths were calculated only for the level 4 high-resolution grid. Map sheets 1–4 show the maximum composite extent of inundation for all scenarios, and the maximum composite flow depths over dry land. The calculated extent of inundation accounts for regional coseismic deformation in the Resurrection Bay area.

First, we modeled tsunami inundation for every megathrust scenario listed in table 3; the corresponding inundation zones are shown in figure 11. Scenario 10 resulted in the worst inundation, followed by scenarios 1, 9, and 8. These scenarios represent ruptures with different but substantial amount of slip in the shallow part of the subduction interface close to the trench. Scenarios 3, 4, and 6 did not result in any inundation because these scenarios substantially uplifted the southern shore of the Kenai Peninsula. Scenario 11, the megathrust earthquake in the Cascadia subduction zone, resulted in minimal inundation.

Next, we analyze the inundation resulting from scenarios with added splay faults. For megathrust scenarios 2, 4, 6, 7, and 8, we made sub-scenarios by adding splay faults with different geometries and surface trace locations (table 5). In figure 12 we display modeling results for the splay fault scenarios. We start by considering inundation lines for selected megathrust-only scenarios (fig. 12A). Figure 12B shows the comparison of base megathrust scenario 2 and the corresponding single scenario that includes an added splay fault as an extension of the Patton Bay fault. The resulting inundation area is significantly larger due to the additional coseismic uplift on the splay fault. Similarly, adding single splay faults to scenarios 4 and 6 results in a substantial increase in inundation (figs. 12C and D).

To our megathrust-only scenario 7 we add three different splay fault sub-scenarios (fig. 12E). All three splay fault sub-scenarios result in an increase in inundation compared to the base scenario. The least significant inundation increase is caused by rupture of the backstop splay fault zone, scenario 7-BS, because the splay fault is located farthest from shore (see fig. 10D). Of the two inferred Patton Bay fault extensions (PBIE1 and PBIE2, figs. 10B and C, respectively), scenario 7-PBIE2 results in a slightly larger inundation because rupture of PBIE2 does not cause as much coseismic uplift as PBIE1.

While adding a PBIE1 rupture to base megathrust scenario 8 does decrease the first wave arrival time (fig. 13E), the splay fault rupture does not increase the total inundation in Seward (fig. 12F). This is likely due to complex wave interactions in the Gulf of Alaska—the initial uplift due to the splay fault rupture produces a wave (with associated wave trough) that interferes with the incoming wave crest generated by megathrust uplift farther out to sea near the seafloor trench.

Finally, we compare how various splay fault locations affect the arrival time of the first wave at Seward. Figure 13 shows time series plots for five megathrust scenarios with added splay faults. Inclu-
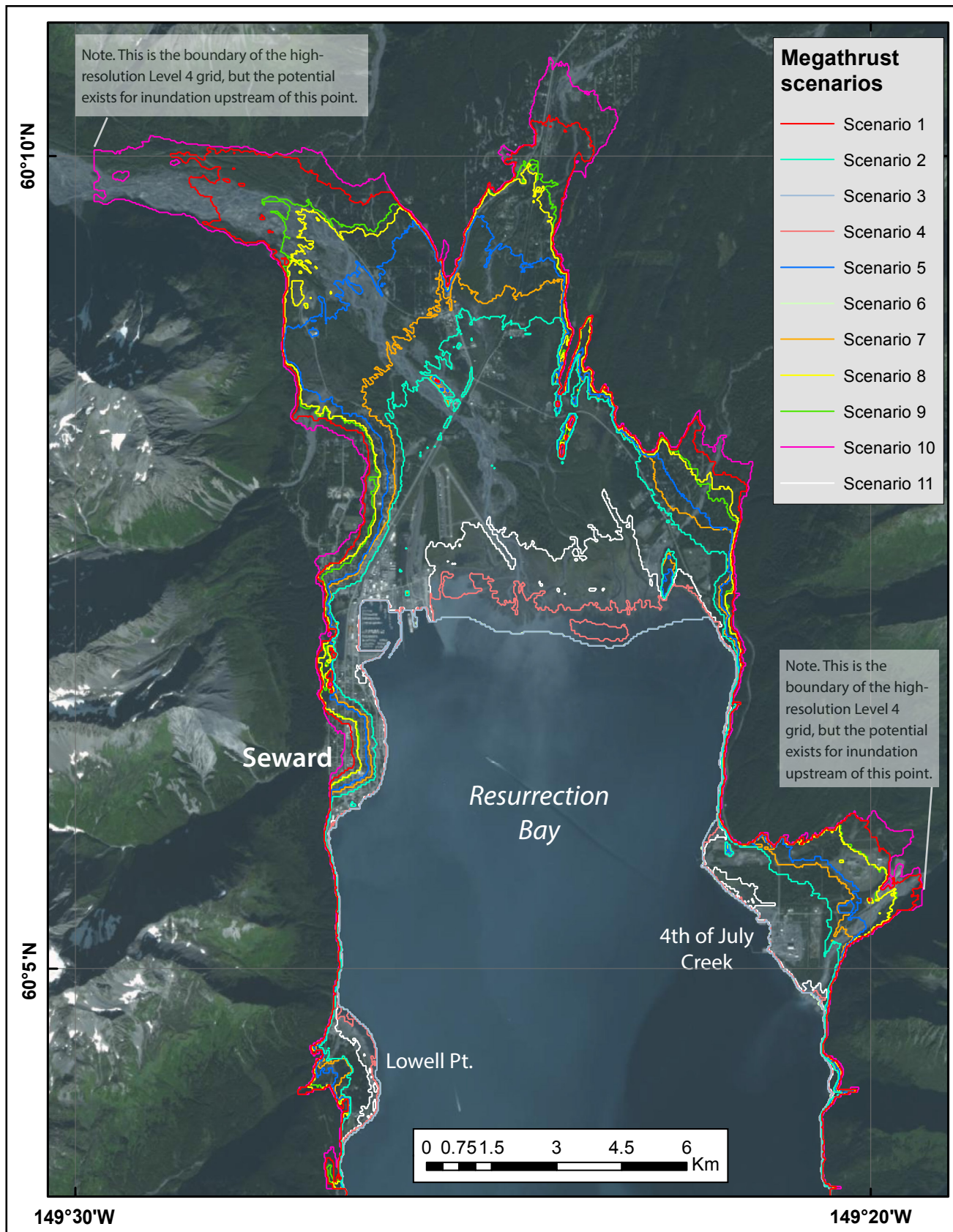
**Figure 11.** Tsunami inundation in upper Resurrection Bay for all megathrust-only scenarios.
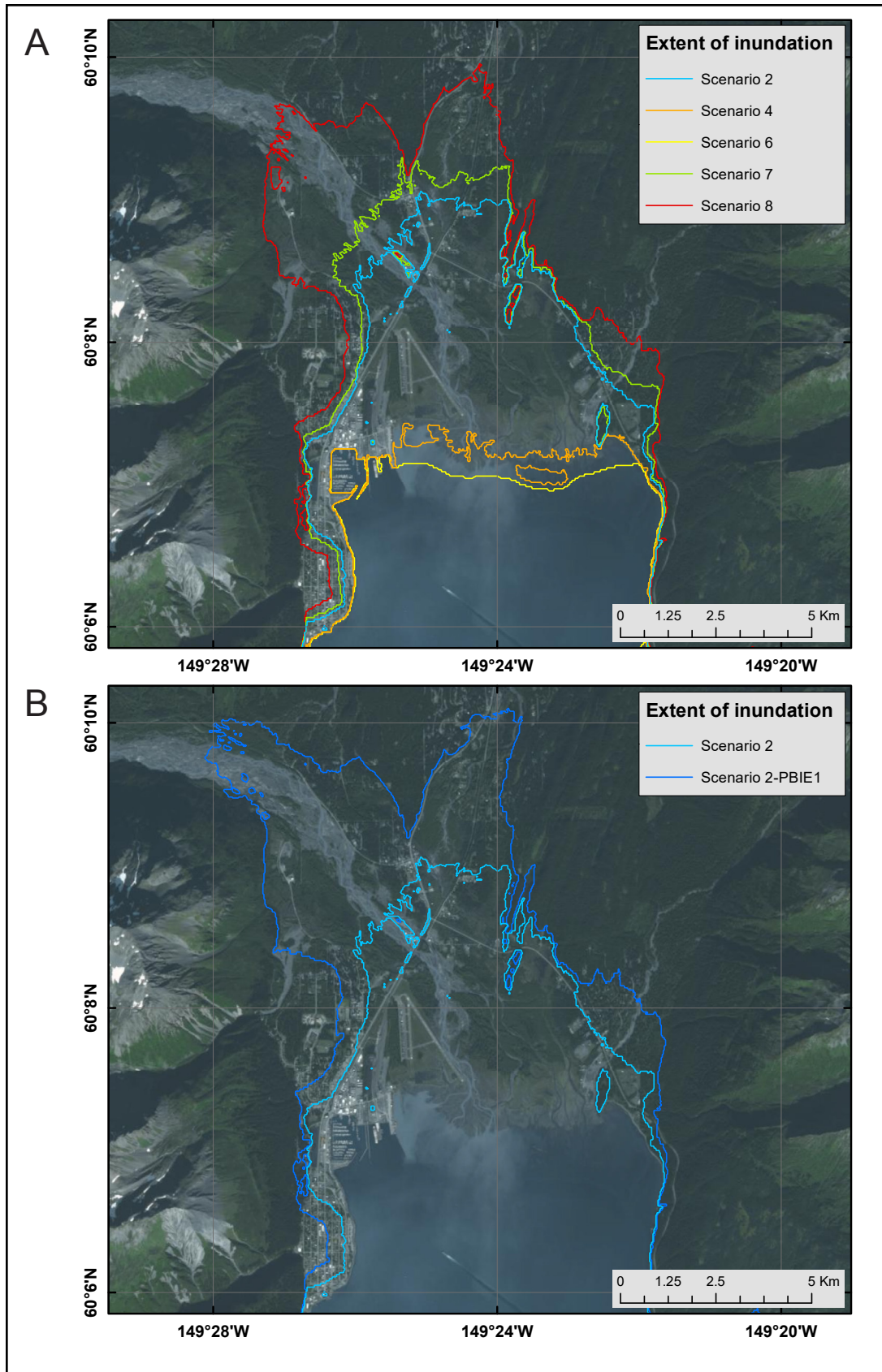
**Figure 12.** Tsunami inundation in upper Resurrection Bay for (**A**) megathrust-only scenarios 2, 4, 6, 7, and 8, and (**B**) splay fault scenario corresponding to base scenario 2.
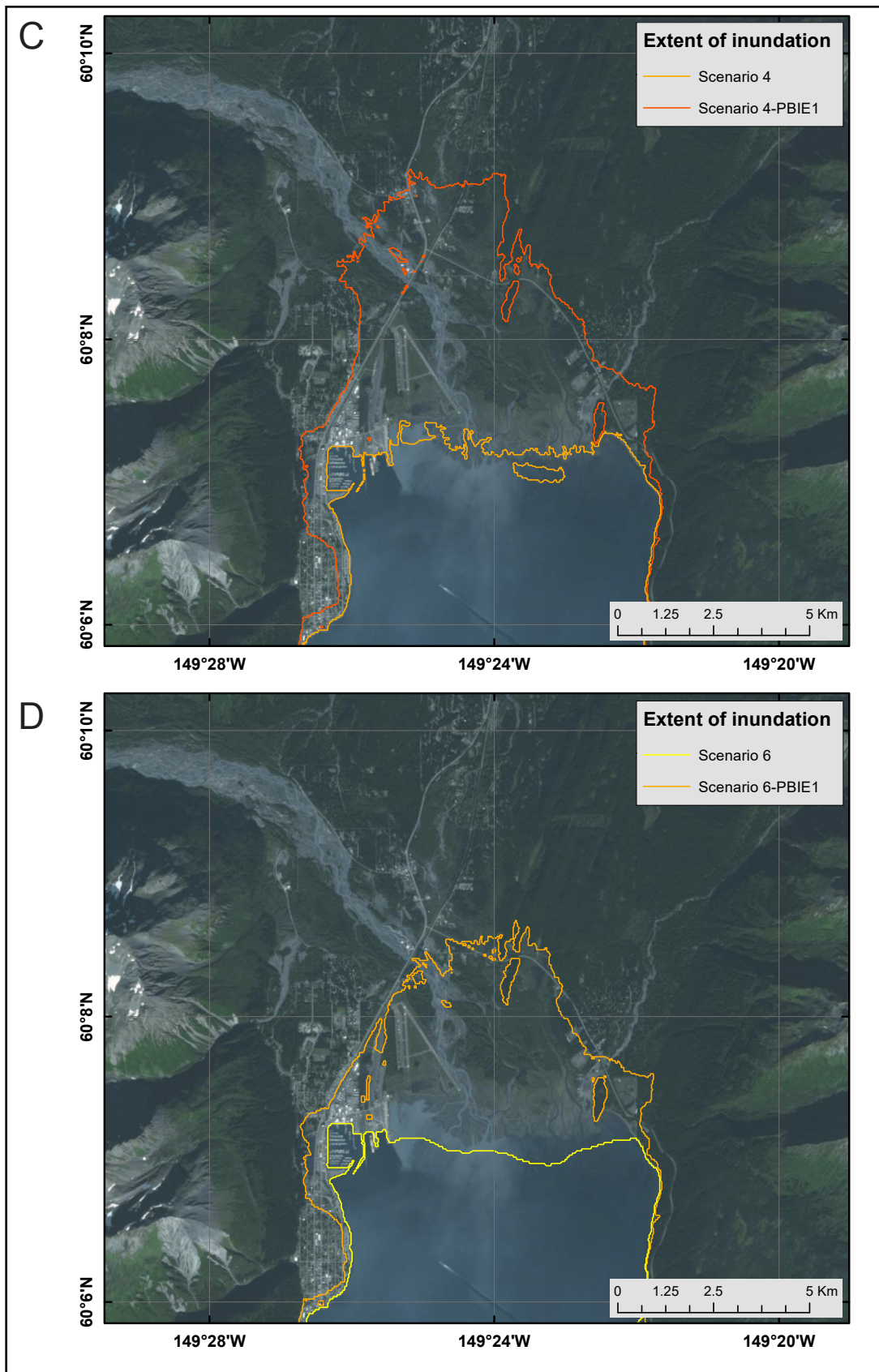
**Figure 12, continued.** Tsunami inundation in upper Resurrection Bay for (**C**) splay fault scenario corresponding to base scenario 4, and (**D**) splay fault scenario corresponding to base scenario 6.
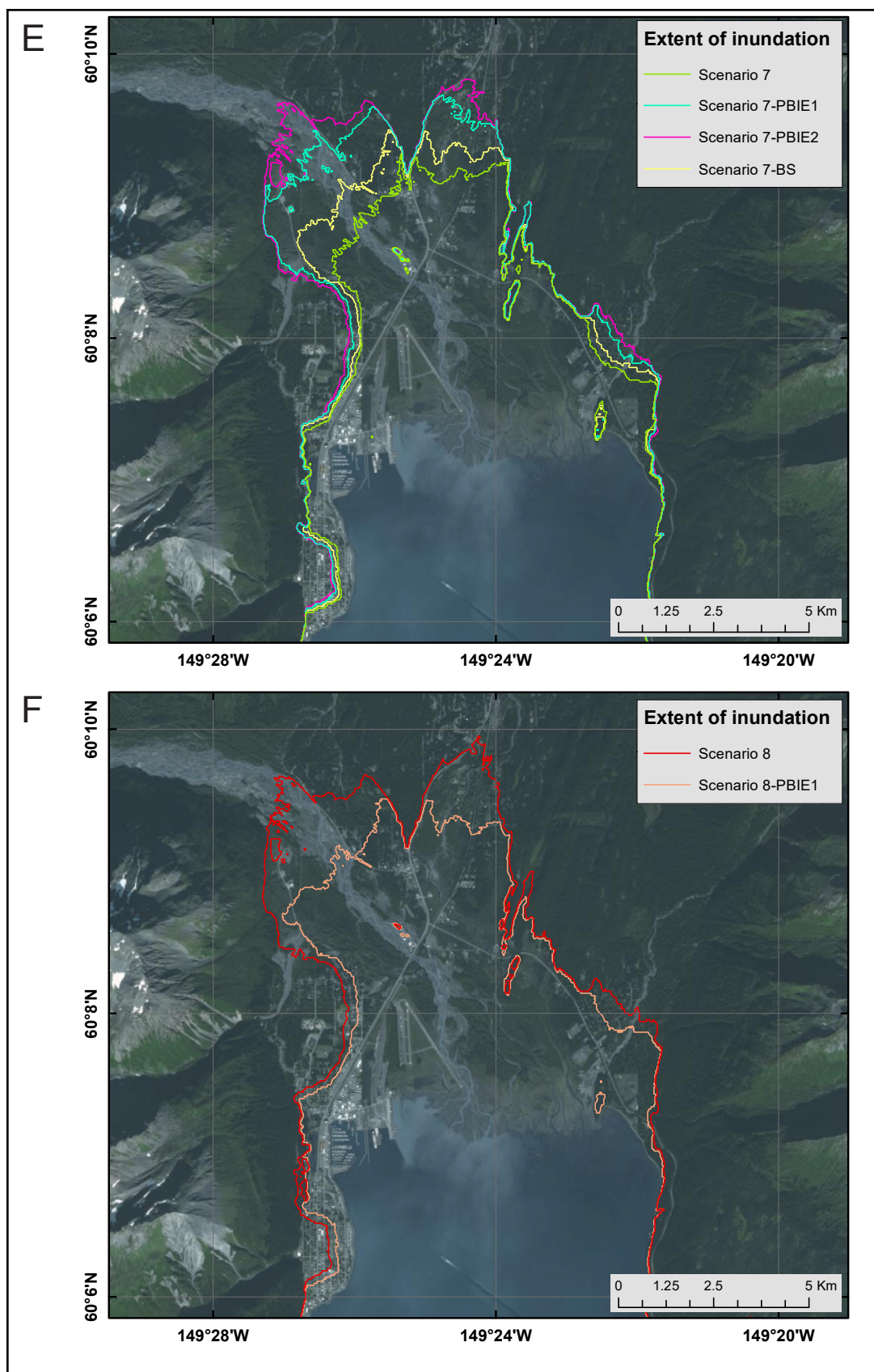
**Figure 12 continued.** Tsunami inundation in upper Resurrection Bay for (**E**) splay fault scenarios corresponding to base scenario 7, and (**F**) splay fault scenario corresponding to scenario 8.
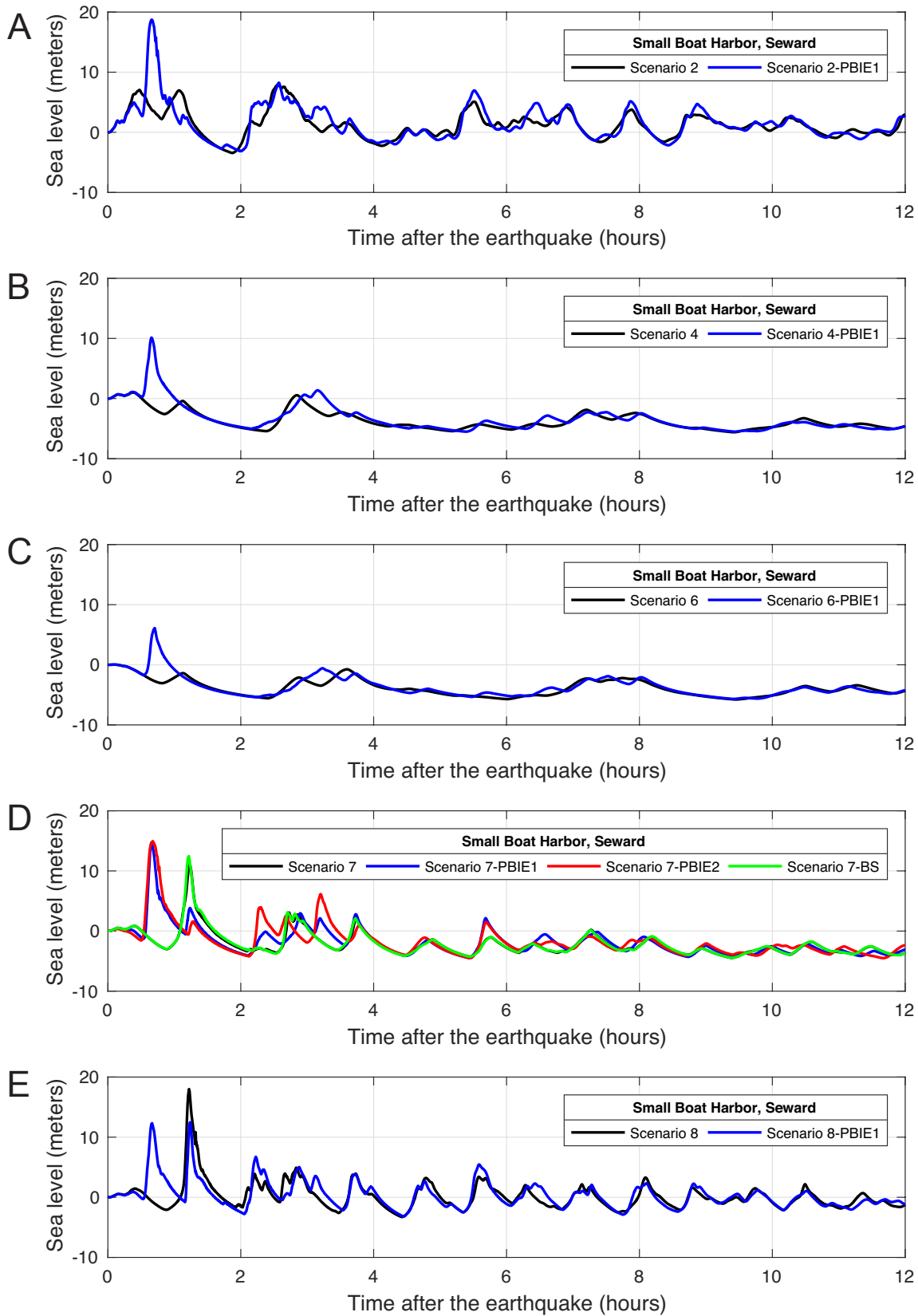
**Figure 13.** Modeled water-level dynamics (from the point of view of an observer standing at the shore) at the Seward Small Boat Harbor for megathrust scenarios 2, 4, 6, 7, and 8, with corresponding splay fault scenarios.

sion of either PBIE1 or PBIE2 splay fault significantly reduces the arrival time of the first wave for all scenarios except scenario 2. In scenario 2-PBIE1 the first wave arrives about 15 minutes later than that in the megathrust-only scenario, albeit with much larger amplitude (fig. 13A). Inclusion of the BS splay fault in scenario 7 does not change the arrival time of the first wave, because the area of coseismic uplift due to the splay fault is very close to that in the megathrust-only scenario (fig. 10D).

The numerical simulations reveal that the first wave could arrive in Seward about 30 minutes after the earthquake. As demonstrated by the time series data shown in supplemental figure A2, significant wave activity could continue in Resurrection Bay for at least 12 hours after the earthquake, and the predicted average time interval between successive waves is about one hour.

Map sheet 1 shows the composite inundation line and flow depths over dry land for upper Resurrection Bay, and map sheets 2, 3, and 4 show this in more detail for the Seward, Lowell Point, and Fourth of July Creek areas, respectively. Please refer to the "Grid Development and Data Sources" section of this report for a description of how the composite flow depth maps and the composite tsunami inundation lines are generated from multiple scenarios. Since scenarios 10, 1, 9, and 8 result in the top four largest inundation zones, they therefore have a sizeable contribution to the composite map.

## SOURCES OF ERRORS AND UNCERTAINTIES

The hydrodynamic model used to calculate propagation and run-up of tectonic tsunamis is a nonlinear, flux-formulated, shallow-water model (Nicolsky and others, 2011) that passed the verification and validation tests required for numerical codes used to produce tsunami inundation maps (Synolakis and others, 2007; NTHMP, 2012). Most of the errors/uncertainties in the numerical predictions originate from the tsunami sources used in the numerical models. Furthermore, our assessment of potential earthquake scenarios is not exhaustive and

represents a best estimate of the locations and sizes of potential tsunami-generating events. It is possible that other unrecognized earthquake scenarios or slope failures could present hazards to populated locations in northern Resurrection Bay and in Seward (Suleimani and others, 2010). However, the scenarios presented in this report are intended to cover the range of potential situations about which the community should be aware.

The spatial resolution of the grid used to calculate tsunami inundation in Resurrection Bay is about 14 m (46 ft) and satisfies NOAA minimum recommended requirements for computation of tsunami inundation (NTHMP, 2010). Although this resolution is high enough to describe major relief features, small topographic features, buildings, and other facilities cannot be resolved accurately by the existing model. We also note that uncertainty in grid-cell elevation/depth propagates into the modeling results and eventually contributes to horizontal uncertainty in the location of the inundation line. One contribution to this uncertainty is the paucity of data in the intertidal zone. However, no established practices exist to directly propagate the DEM uncertainty into the uncertainty of the inundation line (Hare and others, 2011). In addition to the uncertainty related to the grid cell elevation/depth, uncertainties in the tsunami source (earthquake and splay fault geometry) are the largest source of error in tsunami modeling efforts. The direction of the incoming waves, their amplitudes, and times of arrival are primarily determined by displacements of the ocean in the source area. Therefore, the inundation modeling results for local sources are especially sensitive to the fine structure of the tsunami source. The modeling process is highly sensitive to errors when the complexity of the source function is combined with its proximity to the coastal zone.

## SUMMARY

We present the results of numerical modeling of earthquake-generated tsunamis for the community of Seward and other locations in northern

Resurrection Bay, Alaska. The earthquake scenarios considered in this report include a range of different earthquake ruptures in the eastern part of the Alaska–Aleutian megathrust. A hypothetical earthquake with maximum slip distributed at depths between 0 and 20 km (12.4 mi) results in "worst case" tsunami inundation for Seward. The maximum predicted overland flow depths in the community range from 10 to 25 m (33 to 82 ft), and the currents in community harbors could be as strong as 25 m/sec (48.6 knots). Dangerous wave activity is expected to last for at least 12 hours after the earthquake.

Each scenario considered is geologically reasonable and presents potential hazards to the communities. Map sheets 1–4, which show the potential extent of inundation and the tsunami flow depths, have been completed using the best information available and are believed to be accurate; however, their preparation required many assumptions. We considered several tsunami scenarios and have provided an estimate of maximum credible tsunami inundation. Actual conditions during a tsunami event may vary from those considered, so the accuracy of predictions based on the modeling presented in this report cannot be guaranteed. The limits of inundation shown should only be used as a guideline for emergency planning and response action. Actual inundated areas will depend on specifics of earthquake deformation, on-land construction, and tide level, and may differ from areas shown on the map. The information on this map is intended to assist state and local agencies in planning for emergency evacuation and tsunami response actions in the event of a major tsunamigenic earthquake. These results are not intended for land-use regulation or building-code development.

## ACKNOWLEDGMENTS

# REFERENCES

Butler, Rhett, 2012, Re-examination of the potential for great earthquakes along the Aleutian island arc with implication for tsunamis in Hawai'i: Seismological Research Letters, v. 83, no. 1, p. 30–39. doi.org/10.1785/gssrl.83.1.29

———2014, Great Aleutian tsunamis: Honolulu, HI, University of Hawai'i at Manoa, Hawai'i Institute of Geophysics & Planetology, Peer-Reviewed Report HIGP-2014-1, 170 p. www.higp.hawaii.edu/reports/2014

Butler, Rhett, Burney, David, and Walsh, David, 2014, Paleo-tsunami evidence on Kaua'i and numerical modeling of a great Aleutian tsunami: Geophysical Research Letters, v. 41, no. 19, p. 6,795–6,802. doi.org/10.1002/2014GL061232

Christensen, D.H., and Beck, S.L., 1994, The rupture process and tectonic implications of the Great 1964 Prince William Sound Earthquake: Pure and Applied Geophysics, v. 142, no. 1, p. 29–53. doi.org/10.1007/BF00875967

Cohen, S.C., and Freymueller, J.T., 2004, Crustal deformation in Southcentral Alaska: The 1964 Prince William sound earthquake sub- duction zone: Advances in Geophysics, v. 47, 1–63.

Department of Commerce, Community, and Economic Development (DCCED)/Division of Community and Regional Affairs (DCRA), 2015, Community Database Online, accessed November 22, 2016. www.commerce.alaska.gov/dcra/DCRAExternal

Dunbar, P.K., and Weaver, C.S., 2008, U.S. states and territories national tsunami hazard assessment—Historical record and sources for waves: Technical Report, National Oceanic and Atmospheric Administration and U.S. Geological Survey, 59 p. nthmp.tsunami.gov/documents/Tsunami_Assessment_Final.pdf

Eberhart-Phillips, Donna, Christensen, D.H., Brocher, T.M., Hansen, Roger, Ruppert, N.A., Haeussler, P.J., and Abers, G.A., 2006, Imaging the transition from Aleutian subduction to Yakutat collision in central Alaska, with local earthquakes and active source data: Journal of Geophysical Research, v. 111, no. B11, p. 303. doi.org/10.1029/2005JB004240

Elliott, Julie, and Freymueller, J.T., 2020, A block model of present-day kinematics of Alaska and western Canada. Journal of Geophysical Research: Solid Earth, v. 125, no. 7. doi.org/10.1130/ 10.1029/2019JB018378

Ferris, Aaron, Abers, G.A., Christensen, D.H., and Veenstra, Elizabeth, 2003, High resolution image of the subducted Pacific(?) plate beneath central Alaska, 50–150 km depth: Earth and Planetary Science Letters, v. 214, no. 3–4, p. 575–588. doi.org/10.1016/S0012-821X(03)00403-5

Fine, I.V., Thomson, R.E., Lupton, L.M., and Mundschutz, Stephen, 2018a, Numerical modeling of an Alaska 1964-type tsunami at the Canadian Coast Guard Base in Seal Cove, British Columbia: Canadian Technical Report of Hydrography and Ocean Sciences 321, Ocean Sciences Division, Fisheries and Oceans Canada, Institute of Ocean Sciences, Sidney, BC.

———2018b, Numerical modeling of an Alaska 1964-type tsunami at the Canadian Coast Guard Base in Victoria, British Columbia: Canadian Technical Report of Hydrography and Ocean Sciences 323, Ocean Sciences Division, Fisheries and Oceans Canada, Institute of Ocean Sciences, Sidney, BC.

Freund, L.B., and Barnett, D.M., 1976, A two-dimensional analysis of surface deformation due to dip-slip faulting: Bulletin of the Seismological Society of America, v. 66, no. 3, p. 667–675.

Freymueller, J.T., Woodard, Hillary, Cohen, S.C., Cross, Ryan, Elliott, Julie, Larsen, C.F., Hreinsdóttir, Sigrún, 2008, Active deformation processes in Alaska, based on 15 years of GPS measurements, in Freymueler, J.T., Haeussler, P.J., Wesson, R.L., and Ekström, Göran, eds., Active Tectonics and Seismic Potential of Alaska: Geophysical Monograph Series: Washington, D.C., American Geophysical Union, p. 1–42. doi.org/10.1029/179GM02

Geist, E.L., and Parsons, Tom, 2006, Probabilistic analysis of tsunami hazards: Natural Hazards, v. 37, no. 3, p. 277–314. doi.org/10.1007/s11069-005-4646-z

Gulick, S.P.S., Reece, R.S., Christenson, G.L., Van Avendonk, H.J.A., Worthington, L.L., and Pavlis, T.L., 2013, Seismic images of the Transition fault and the unstable Yakutat–Pacific–North American triple junction: Geology, v. 41, no. 5, p. 571–574. doi.org/10.1130/G33900.1

Haeussler, P.J., Lee H.J., Ryan H.F., Labay K., Kayen R.E., Hampton M.A., and Suleimani E.N., 2007, Submarine slope failures near Seward, Alaska, during the M9.2 1964 earthquake, in Lykousis V, Sakellariou D., and Locat J., eds., Submarine Mass Movements and their consequences, Springer, .p 269–278.

Hare, Rob, Eakins, B.W., and Amanate, Christopher, 2011, Modelling bathymetric uncertainty: International Hydrographic Review, p. 31–42. journals.lib.unb.ca/index.php/ihr/article/view/20888

Hayes, Gavin, 2018, Slab2-A Comprehensive Subduction Zone Geometry Model: U.S. Geological Survey data release. doi.org/10.5066/F7PV6JNV

Heidarzadeh, Mohammad, 2011, Major tsunami risk from splay faulting, in Mörner, N.A., ed., The tsunami threat: research and technology, p. 67–80. doi.org/10.5772/13375

Johnson, J.M., Satake, Kenji, Holdahl, S.R., and Sauber, Jeanne, 1996, The 1964 Prince William Sound earthquake—Joint inversion of tsunami waveforms and geodetic data: Journal of Geophysical Research, v. 101, no. B1, p. 523–532. doi.org/10.1029/95JB02806

Kanamori, Hiroo, 1970, The Alaska earthquake of 1964—Radiation of long-period surface waves and source mechanism: Journal of Geophysical Research, v. 75, no. 26, p. 5,029–5,040. doi.org/10.1029/JB075i026p05029

Kelsey, H.M., Witter, R.C., Engelhart, S.E., Briggs, Richard, Nelson, Alan, Haeussler, P.J., Corbett, D.R., 2015, Beach ridges as paleoseismic indicators of abrupt coastal subsidence during subduction zone earthquakes, and implications for Alaska–Aleutian subduction zone paleoseismology, southeast coast of the Kenai Peninsula, Alaska, Quaternary Science Reviews, v. 113, p. 147–158. doi.org/10.1016/j.quascirev.2015.01.006

Kirby, Stephen, Scholl, David, von Huene, Roland, and Wells, Ray, 2013, Alaska earthquake source for the SAFRR tsunami scenario, chapter B, in Ross, S.L., and Jones, L.M., eds., The SAFRR (Science Application for Risk Reduction) Tsunami Scenario: U.S. Geological Survey Open-File Report 2013–1170, 40 p. pubs.usgs.gov/of/2013/1170/b/

Labay, K.A., and Haeussler, P.J., 2008, Combined high-resolution LIDAR topography and multibeam bathymetry for upper Resurrection Bay, Seward, Alaska. U.S. Geological Survey Digital Data Series.

Lander, J.F., 1996, Tsunamis affecting Alaska, 1737–1996: Boulder, CO, National Oceanic and Atmospheric Administration, National Geophysical Data Center (NGDC), Key to Geophysical Research Documentation, v. 31, 155 p. ftp.ngdc.noaa.gov/hazards/publications/Kgrd-31.pdf

Larsen, C.F., Motyka, R.J., Freymueller, J.T, Echelmeyer, K.A., and Ivins, E.R., 2004, Rapid uplift of southern Alaska caused by recent ice loss: Geophysical Journal International, v. 158, no. 3, p. 1,118–1,133. doi.org/10.1111/j.1365-246X.2004.02356.x

Lemke, R.W., 1967, Effects of the Earthquake of March 27, 1964, at Seward, Alaska. U.S. Geological Survey Professional Paper 542-E, 48 p.

Li, Shaoyang, Moreno, Marcos, Rosenau, Matthias, Melnick, Daniel, and Oncken, Onno, 2014, Splay fault triggering by great subduction earthquakes inferred from finite element models: Geophysical Research Letters, v. 41, no. 2, p. 385–391. doi.org/10.1002/2013GL058598

Liberty, L.M., Brothers, D.S., and Haeussler, P.J., 2019, Tsunamigenic splay faults imply a long-term asperity in southern Prince William Sound, Alaska: Geophysical Research Letters, v. 46, p. 3,764–3,772. doi.org/10.1029/2018GL081528

Liberty, L.M., Finn, S.P., Haeussler, P.J., Pratt, T.L., and Peterson, Andrew, 2013, Megathrust splay faults at the focus of the Prince William Sound asperity, Alaska, Journal of Geophysical Research, 118, p. 1–14. doi.org/10.1002/jgrb.50372

Lotto, G.C., Jeppson, T.N., and Dunham, E.M., 2019, Fully Coupled Simulations of Megathrust Earthquakes and Tsunamis in the Japan Trench, Nankai Trough, and Cascadia Subduction Zone: Pure and Applied Geophysics, v. 176, p. 4,009–4,041. doi.org/10.1007/s00024-018-1990-y

National Centers for Environmental Information (NCEI/WDS), in progress, Global historical tsunami database at NCEI, 2100 BC to present (interactive map): National Centers for Environmental Information, NOAA. doi.org/10.7289/V5PN93H7

National Tsunami Hazard Mapping Program (NTHMP), 2010, Guidelines and best practices for tsunami inundation modeling for evacuation planning: National Oceanic and Atmospheric Administration (NOAA), NTHMP Mapping & Modeling Subcommittee.

———2012, Proceedings and results of the 2011 NTHMP Model Benchmarking Workshop: Boulder, CO, U.S. Department of Commerce/NOAA/NTHMP, NOAA Special Report, 436 p. nthmp.tsunami.gov

Nicolsky, D.J., Suleimani, E.N., Combellick, R.A., and Hansen, R.A., 2011, Tsunami inundation maps of Whittier and western Passage Canal, Alaska: Alaska Division of Geological & Geophysical Surveys Report of Investigation 2011-7, 65 p. doi.org/10.14509/23244

Nicolsky, D.J., Suleimani, E.N., Freymueller, J.T., and Koehler, R.D., 2015, Tsunami inundation maps of Fox Islands communities, including Dutch Harbor and Akutan, Alaska: Alaska Division of Geological & Geophysical Surveys Report of Investigation 2015-5, 67 p., 2 sheets, scale 1:12,500. doi.org/10.14509/29414

Nicolsky, D.J., Suleimani, E.N., Haeussler, P.J., Ryan, H.F., Koehler, R.D., Combellick, R.A., and Hansen, R.A., 2013, Tsunami inundation maps of Port Valdez, Alaska: Alaska Division of Geological & Geophysical Surveys Report of Investigation 2013-1, 77 p., 1 sheet, scale 1:12,500. doi.org/10.14509/25055

Nicolsky, D.J., Suleimani, E.N., and Hansen, R.A., 2011, Validation and verification of a numerical model for tsunami propagation and runup: Pure and Applied Geophysics, v. 168, no. 6, p. 1,199–1,222. doi.org/10.1007/s00024-010-0231-9

Nicolsky, D.J., Suleimani, E.N., and Koehler, R.D., 2014, Tsunami inundation maps of Cordova and Tatitlek, Alaska: Alaska Division of Geological & Geophysical Surveys Report of Investigation 2014-1, 49 p. doi.org/10.14509/27241

———2016, Tsunami inundation maps for the communities of Chignik and Chignik Lagoon, Alaska: Alaska Division of Geological & Geophysical Surveys Report of Investigation 2016-8, 48 p., 2 sheets, scale 1:12,500. doi.org/10.14509/29675

Nicolsky, D.J., Suleimani, E.N., Koehler, R.D., and Salisbury, J.B., 2017, Tsunami inundation maps for Juneau, Alaska: Alaska Division of Geological & Geophysical Surveys Report of Investigation 2017-9, 66 p., 5 sheets. doi.org/10.14509/29741

Nicolsky, D.J., Suleimani, E.N., and Salisbury, J.B., 2018, Tsunami inundation maps for Skagway and Haines, Alaska: Alaska Division of Geological & Geophysical Surveys Report of Investigation 2018-2, 69 p., 3 sheets. doi.org/10.14509/30029

Okada, Yoshimitsu, 1985, Surface deformation due to shear and tensile faults in a half-space: Bulletin of the Seismological Society of America, v. 75, no. 4, p. 1,135–1,154.

Oppenheimer, Michael, Glavovic, B.C., Hinkel, Jochen, van de Wal, Roderik, Magnan, A.K., Abd-Elgawad, Amro, Cai, Rongshuo, Cifuentes-Jara, Miguel, DeConto, R.M., Ghosh, Tuhin, Hay, John, Isla, Federico, Marzeion, Ben, Meyssignac, Benoit, Sebesvari, Zita, 2019, Sea level rise implications for low-lying islands, coasts and communities, *in* Pörtner, H.-O., Roberts, D.C., Masson-Delmotte, V., Zhai, P., Tignor, M., Poloczanska, E., Mintenbeck, K., Alegría, A., Nicolai, M., Okem, A., Petzoid, J., Rama, B., Weyer, N.M., eds., IPCC Special Report on the ocean and cryosphere in a changing climate. www.ipcc.ch/site/assets/uploads/sites/3/2019/11/08_SROCC_Ch04_FINAL.pdf

Plafker, George, 1965, Tectonic deformation associated with the 1964 Alaska earthquake: Science, v. 148, no. 3,678 p. 1,675–1,687.

———1967, Surface faults on Montague Island associated with the 1964 Alaska earthquake: U.S. Geological Survey Professional Paper 543-G, p. G1–G42. pubs.usgs.gov/pp/0543g/

———1969, Tectonics: U.S. Geological Survey Professional Paper 543-I, p. G1–G74.

Plafker, George, Kachadoorian, Reuben, Eckel, E.B., and Mayo, L.R., 1969, Effects of the earthquake of March 27, 1964, on various communities: U.S. Geological Survey Professional Paper 542-G, 50 p. pubs.usgs.gov/pp/0542g/

Rabinovich, A.B., Thomson, R.E., Krassovski, M.V., Stephenson, F.E., and Sinnott, D.C., 2019, Five Great Tsunamis of the 20th Century as Recorded on the Coast of British Columbia: Pure and Applied Geophysics, v. 176, p. 2,887–2,924. doi.org/10.1007/s00024-019-02133-3

Ryan, Holly, von Huene, Roland, Scholl, Dave, and Kirby, Steve, 2012, Tsunami hazards to U.S. coasts from giant earthquakes in Alaska: Eos AGU, v. 93, no. 19, 185 p.

Savage, J.C., Plafker, George, Svarc, J.L., and Lisowski, Michael, 2014, Continuous uplift near the seaward edge of the Prince William Sound megathrust: Middleton Island, Alaska, JGR Solid Earth, v. 119, no. 7, p. 6,067–6,079. doi.org/10.1002/2014JB011127

Savage, J.C., Svarc, J.L., and Lisowski, Michael, 2015, Strain accumulation across the Prince William Sound asperity, Southcentral Alaska, JGR Solid Earth, v. 120, p. 1,820–1,832. doi.org/10.1002/ 2014JB011652

Shirzaei, Manoochehr, Freymueller, Jeffrey, Törnqvist, T.E., Galloway, D.L., Dura, Tina, and Minderhoud, P.S.J., 2021, Measuring, modelling and projecting coastal land subsidence: Nature Reviews Earth & Environment, no. 2, p. 40–58. doi.org/10.1038/s43017-020-00115-x

Suleimani, E.N., Combellick, R.A., Marriott, D., Hansen, R.A., Venturato, A.J., and Newman, J.C., 2005, Tsunami hazard maps of the Homer and Seldovia areas, Alaska: Alaska Division of Geological & Geophysical Surveys Report of Investigation 2005-2, 28 p., 2 sheets, scale 1:12,500. doi.org/10.14509/14474

Suleimani, E.N., Hansen, R.A, and Haeussler, P.J., 2009, Numerical study of tsunami generated by multiple submarine slope failures in Resurrection Bay, Alaska, during the M9.2 1954 earthquake: Pure and Applied Geophysics, v. 166, p. 131–152. doi.org/10.1007/s00024-004-0430-3

Suleimani, E.N., Nicolsky, D.J., Haeussler, P.J., and Hansen, R.A., 2011, Combined effects of tectonic and landslide-generated tsunami runup at Seward, Alaska, during the M9.2 1964 earthquake: Pure and Applied Geophysics, v. 168, p. 1,053-1,074. doi.org/10.1007/s00024-010-0228-4

Suleimani, E.N., Nicolsky, D.J., and Koehler, R.D., 2013, Tsunami inundation maps of Sitka, Alaska: Alaska Division of Geological & Geophysical Surveys Report of Investigation 2013-3, 76 p., 1 sheet, scale 1:250,000. doi.org/10.14509/26671

———2015, Tsunami inundation maps of Elfin Cove, Gustavus, and Hoonah, Alaska: Alaska Division of Geological & Geophysical Surveys Report of Investigation 2015-1, 79 p. doi.org/10.14509/29404

———2017, Updated tsunami inundation maps of the Kodiak area, Alaska: Alaska Division of Geological & Geophysical Surveys Report of Investigation 2017-8, 38 p., 10 sheets. doi.org/10.14509/29740

Suleimani, E.N., Nicolsky, D.J., Koehler, R.D., Freymueller, J.T., and Macpherson, A.E., 2016, Tsunami inundation maps for King Cove and Cold Bay communities, Alaska: Alaska Division of Geological & Geophysical Surveys Report of Investigation 2016-1, 73 p., 2 sheets, scale 1:12,500. doi.org/10.14509/29565

Suleimani, E.N., Nicolsky, D.J., West, D.A., Combellick, R.A., and Hansen, R.A., 2010, Tsunami inundation maps of Seward and northern Resurrection Bay, Alaska: Alaska Division of Geological & Geophysical Surveys Report of Investigation 2010-1, 47 p., 3 sheets, scale 1:12,500. doi.org/10.14509/21001

Synolakis, C.E., Bernard, E.N., Titov, V.V., Kânoğlu, U., and González, F.I., 2007, Standards, criteria, and procedures for NOAA evaluation of tsunami numerical models: National Oceanic and Atmospheric Administration (NOAA)/Pacific Marine Environmental Laboratory (PMEL) Technical Memorandum OAR PMEL-135, 55 p. www.pmel.noaa.gov/pubs/PDF/syno3053/syno3053.pdf

Von Huene, Roland, Miller, J.J., and Krabbenhoeft, Anne, 2021, The Alaska convergent margin backstop splay fault zone, a potential large tsunami generator between the frontal prism and continental framework: Geochemistry, Geophysics, Geosystems, v. 22, no. 1. doi.org/10.1029/2019GC008901

Wang, Kelin, Sun, Tianhaozhe, Brown, Lonn, Hino, Ryota,Tomita, Fumiaki, Kido, Moyoyuki, Iinuma, Takeshi, Kodaira, Shuichi, and Fujiwara,Toshiya, 2018, Learning from crustal deformation associated with the M9 2011 Tohoku-oki earthquake: Geosphere, v. 14, no. 2, p. 552–571. doi.org/10.1130/GES01531.1

Wang, Kelin, and Tréhu, A.M., 2016, Invited review paper: Some outstanding issues in the study of great megathrust earthquakes—The Cascadia example: Journal of Geodynamics, v. 98, p. 1–18.

Wang, Kelin, Wells, R.E., Mazzotti, Stephane, Hyndman, R.D., and Sagiya, Takeshi, 2003, A revised dislocation model of interseismic deformation of the Cascadia subduction zone: Journal of Geophysical Research, v. 108, no. B1, p. 2,026–2,038. doi.org/10.1029/2001JB001227

Wendt, James, Oglesby, D.D., and Geist, E.L., 2009, Tsunamis and splay fault dynamics: Geophysical Research Letters, v. 36, no. 15. doi.org/10.1029/2009GL038295

Worthington, L.L., Gulick, S.P.S., and Pavlis, T.L., 2010, Coupled stratigraphic and structural evolution of a glaciated orogenic wedge, offshore St. Elias orogen, Alaska: Tectonics, v. 29, no. 6, TC6013. doi.org/10.1029/2010TC002723

Worthington, L.L., van Avendonk, H.J.A., Gulick, S.P.S., Christeson, G.L., and Pavlis, T.L., 2012, Crustal structure of the Yakutat terrane and the evolution of subduction and collision in southern Alaska: Journal of Geophysical Research, v. 117, no. B1. doi.org/10.1029/2011JB008493

Zweck, Chris, Freymueller, J.T., Cohen, S.C., 2002, Three-dimensional elastic dislocation modeling of the postseismic response to the 1964 Alaska earthquake: Journal of Geophysical Research, v. 107, no. B4. doi.org/10.1029/2001JB000409

# APPENDIX A
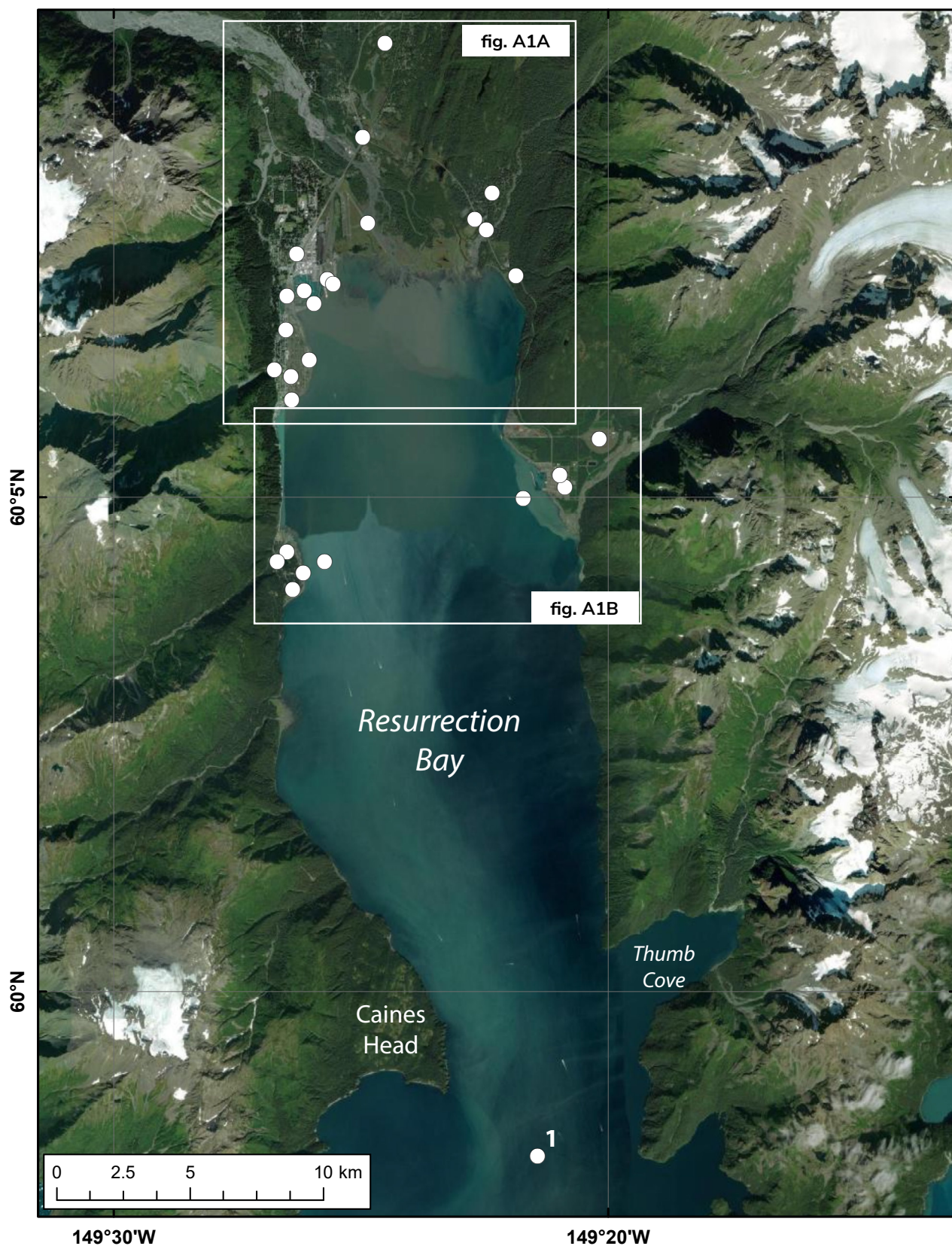


**Figure A1.** Locations of time series points in and around Seward. The longitude and latitude locations of the time series points are listed in table A1.
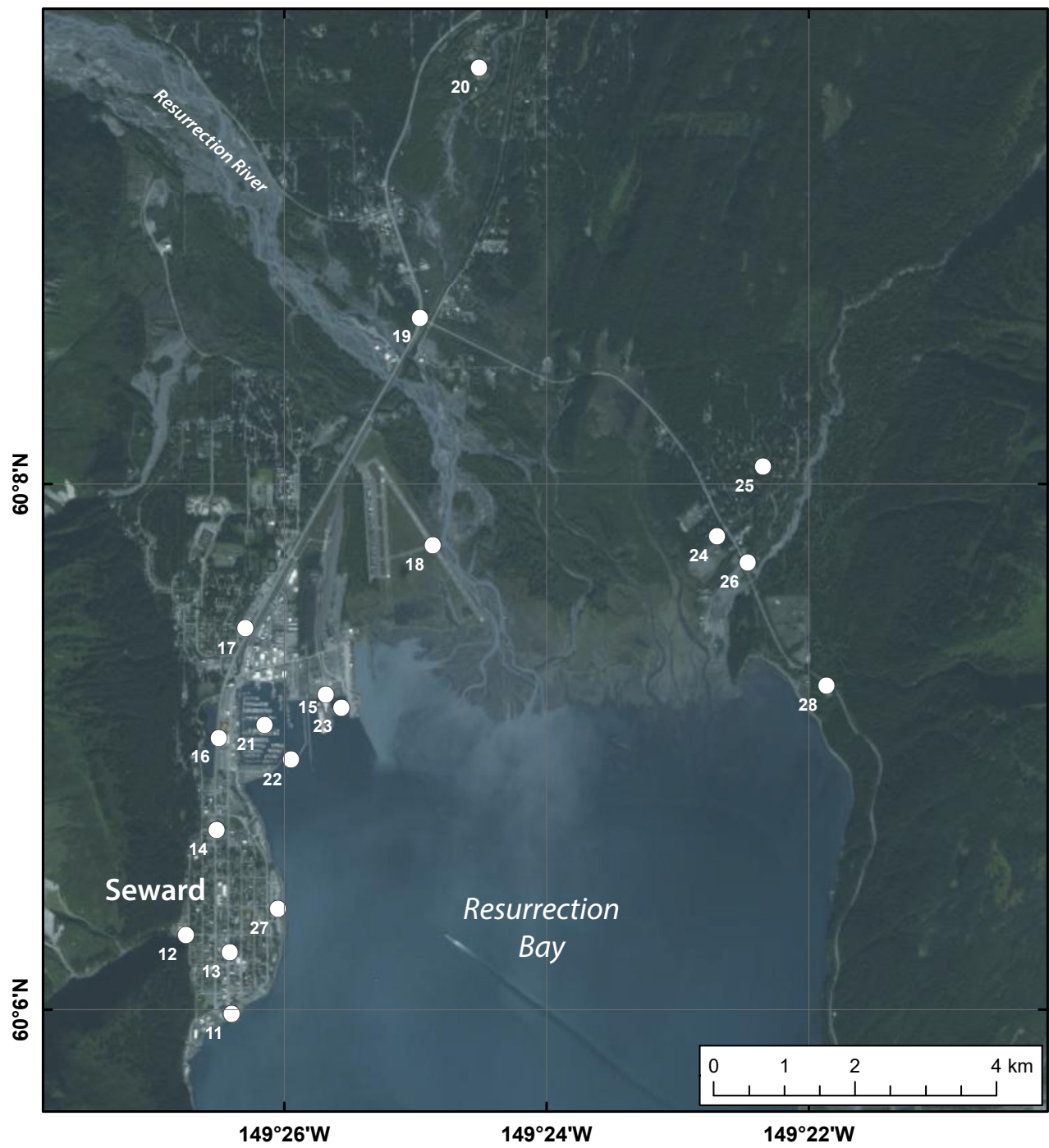
**Figure A1. A.** Locations of time series points in and around Seward. The longitude and latitude locations of the time series points are listed in table A1.
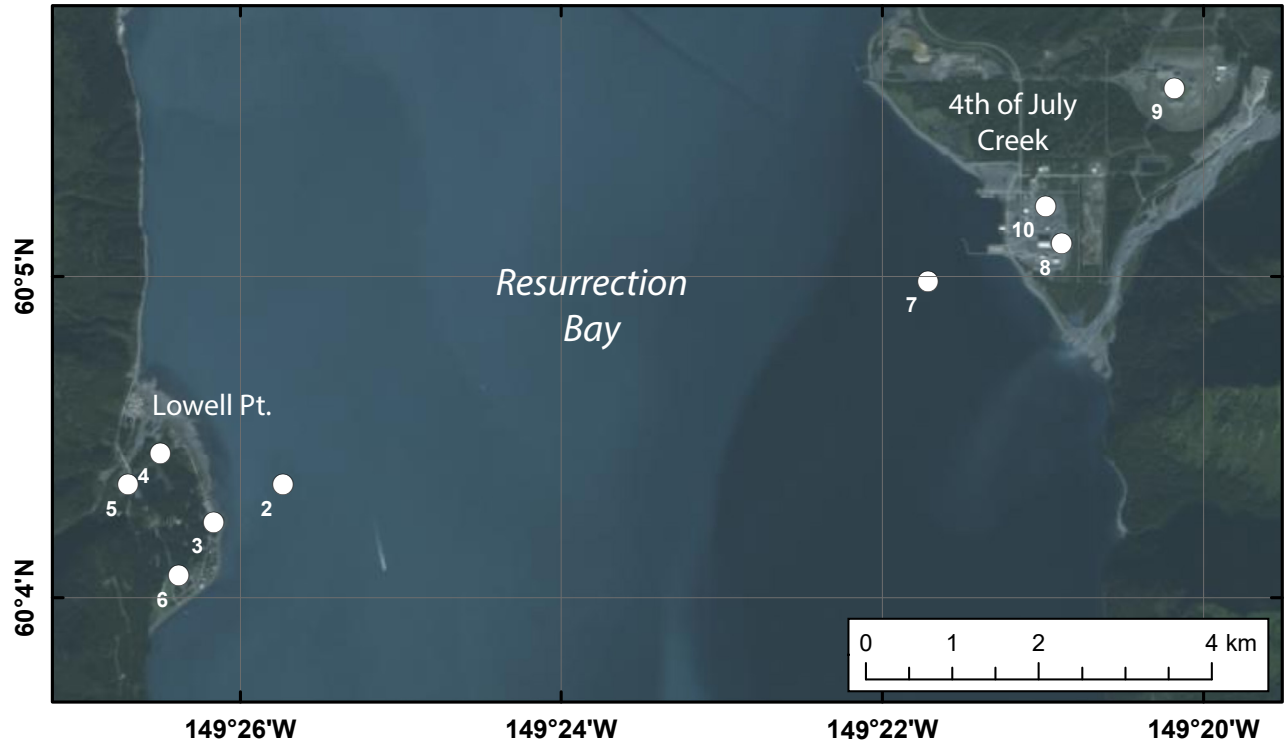
**Figure A1. B.** Locations of time series points in and around Seward. The longitude and latitude locations of the time series points are listed in table A1.
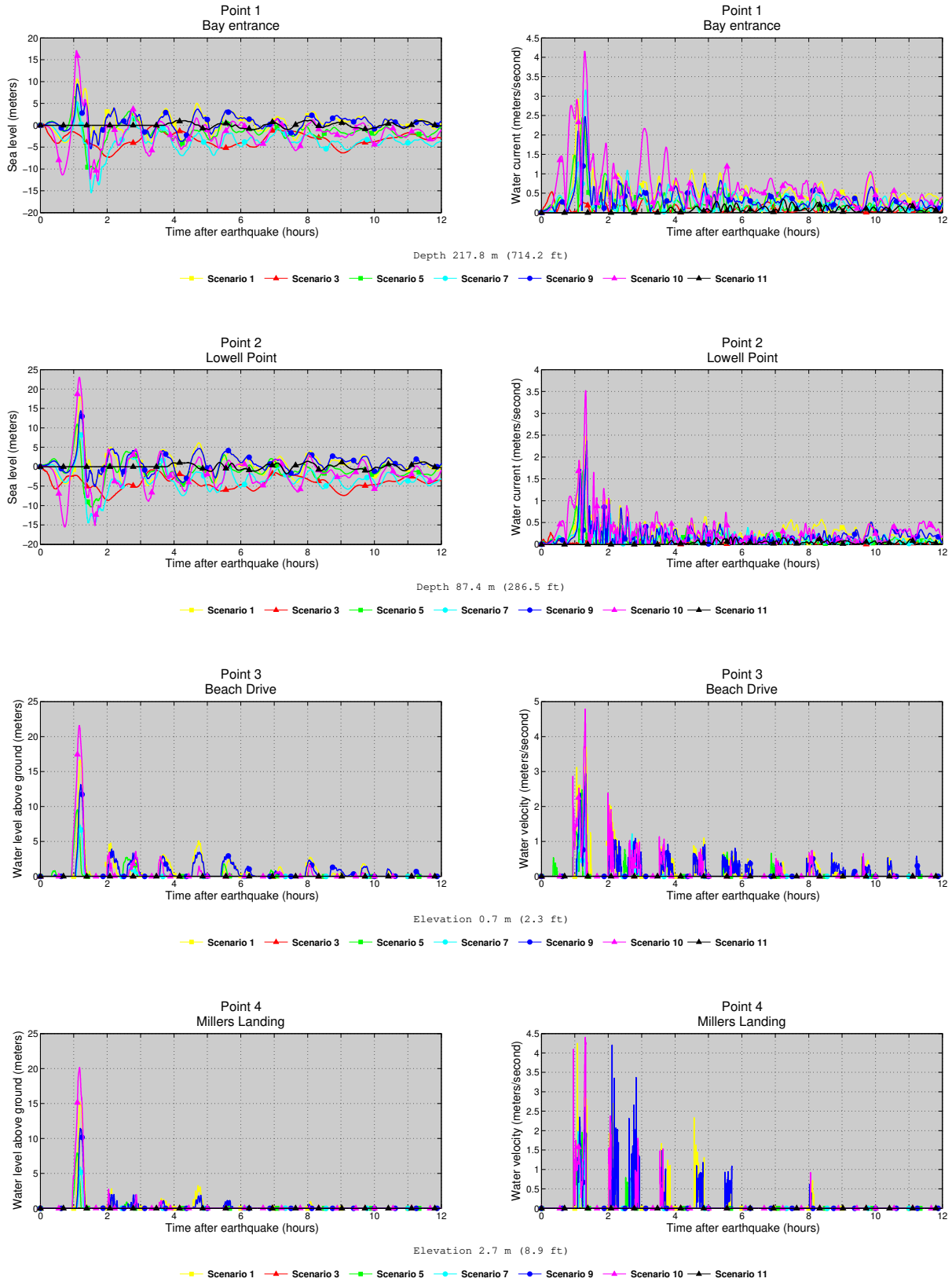
**Figure A2.** Time series of water level (left column) and velocity (right column) for selected scenarios at locations shown in figure A1. Elevations of onshore locations and ocean depth at offshore locations are given based on the pre-earthquake MHHW datum.

**Figure A2, continued.** Time series of water level (left column) and velocity (right column) for selected scenarios at locations shown in figure A1. Elevations of onshore locations and ocean depth at offshore locations are given based on the pre-earthquake MHHW datum.

**Figure A2, continued.** Time series of water level (left column) and velocity (right column) for selected scenarios at locations shown in figure A1. Elevations of onshore locations and ocean depth at offshore locations are given based on the pre-earthquake MHHW datum.

**Figure A2, continued.** Time series of water level (left column) and velocity (right column) for selected scenarios at locations shown in figure A1. Elevations of onshore locations and ocean depth at offshore locations are given based on the pre-earthquake MHHW datum.

**Figure A2, continued.** Time series of water level (left column) and velocity (right column) for selected scenarios at locations shown in figure A1. Elevations of onshore locations and ocean depth at offshore locations are given based on the pre-earthquake MHHW datum.

**Figure A2, continued.** Time series of water level (left column) and velocity (right column) for selected scenarios at locations shown in figure A1. Elevations of onshore locations and ocean depth at offshore locations are given based on the pre-earthquake MHHW datum.

**Figure A2, continued.** Time series of water level (left column) and velocity (right column) for selected scenarios at locations shown in figure A1. Elevations of onshore locations and ocean depth at offshore locations are given based on the pre-earthquake MHHW datum.

**Table A1.** Location of time series points in Seward. The maximum water depth above ground is provided for onshore locations (S), whereas the maximum water level above the pre-earthquake MHHW is provided for offshore (O) locations.
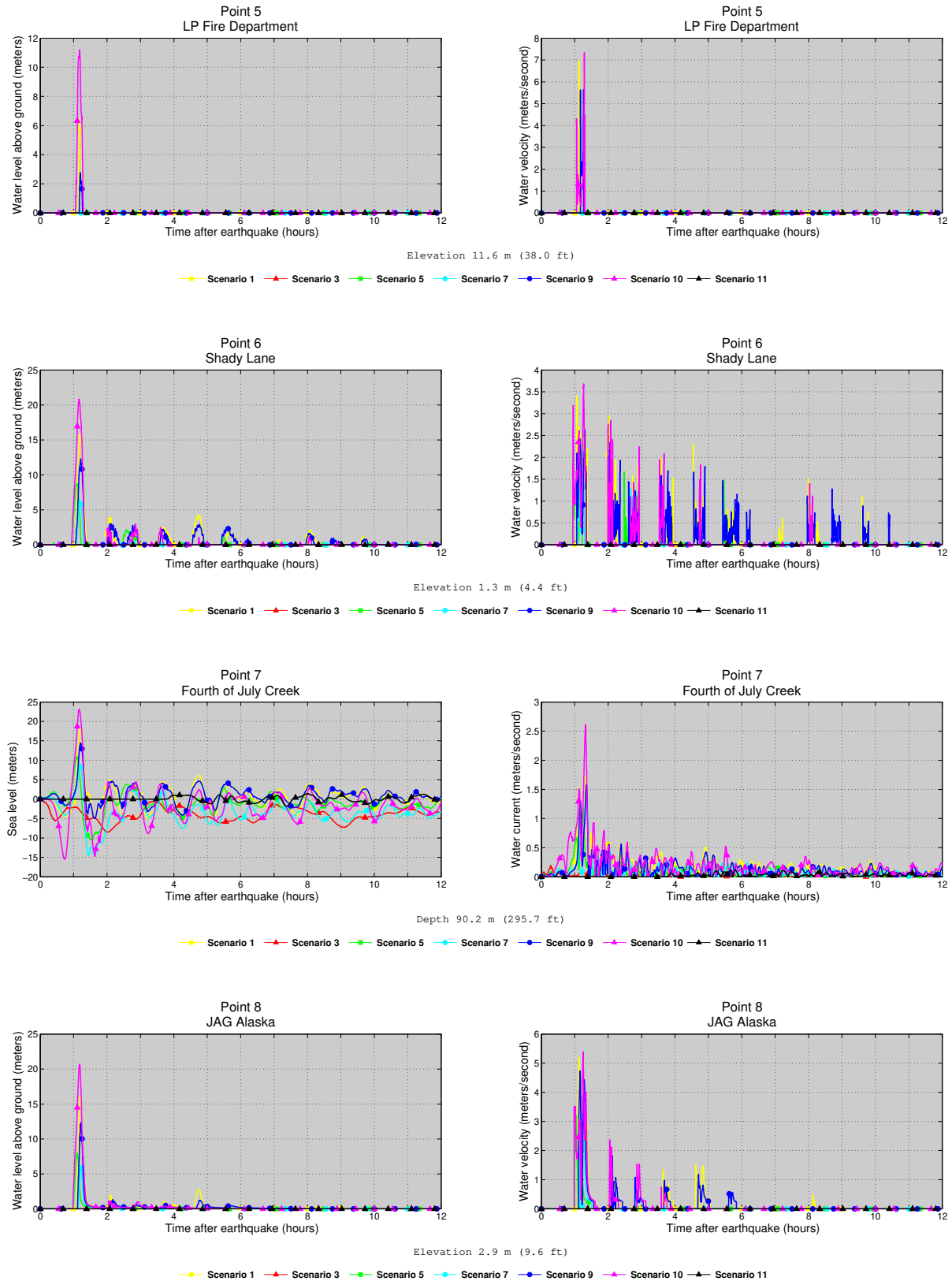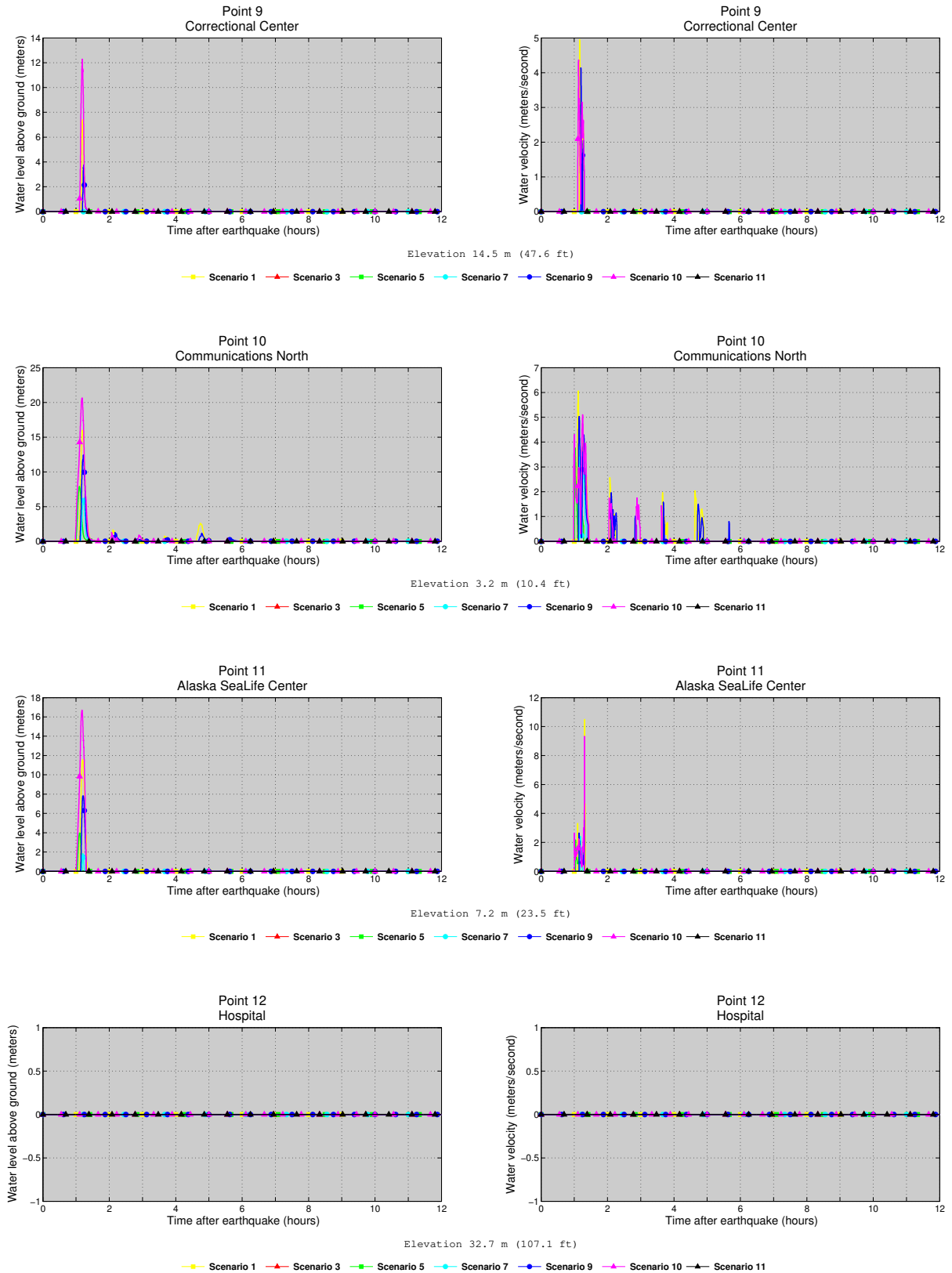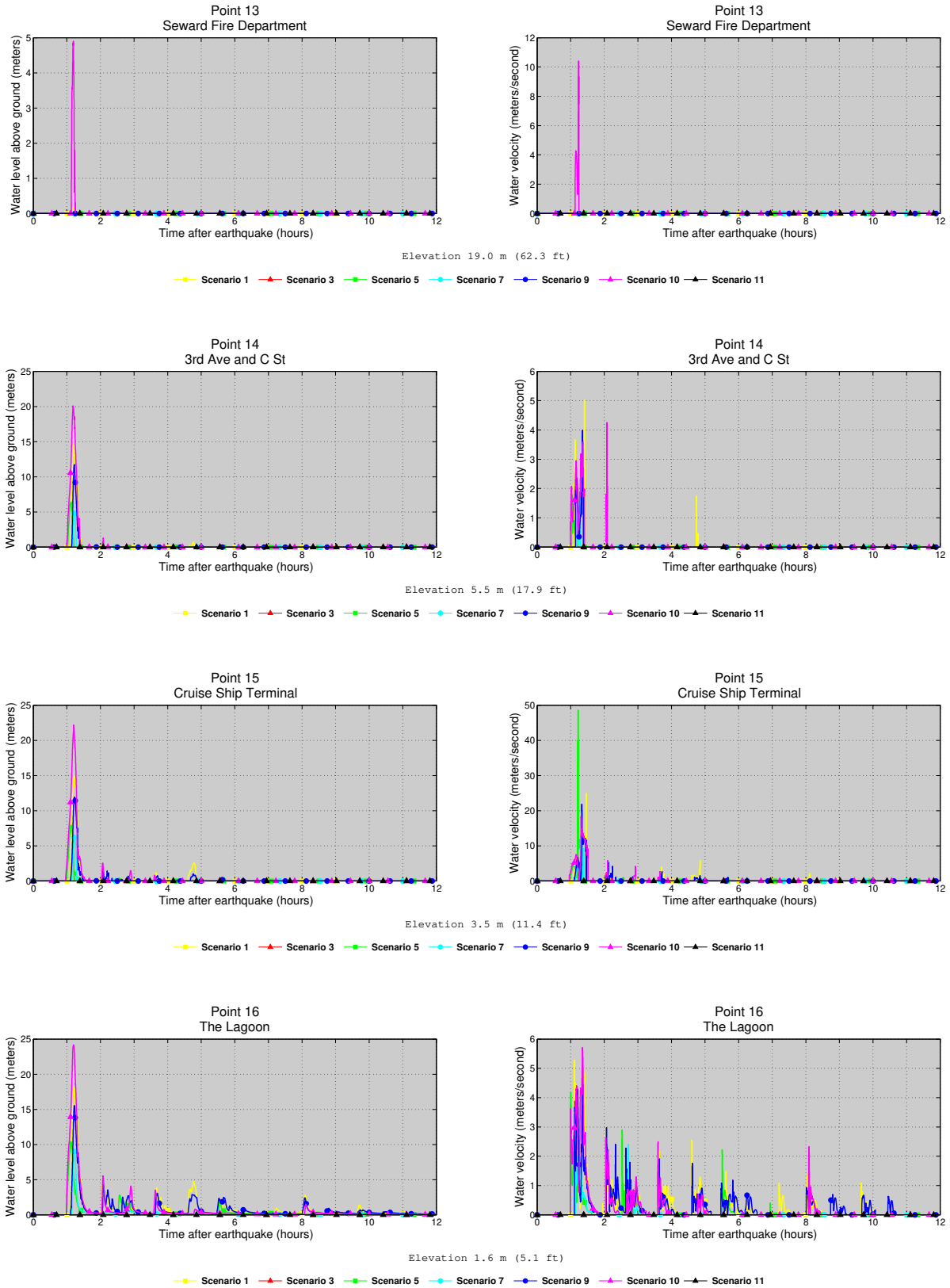
| # | Location | S/O | Longitude (°W) | Latitude (°N) | Min. Elevation/ Depth (m) |
|---|---|---|---|---|---|
| 1 | Bay entrance | O | -149.357222 | 59.972222 | 212.5 |
| 2 | Lowell Point | O | -149.428889 | 60.072500 | 82.5 |
| 3 | Beach Drive | S | -149.436111 | 60.070556 | 0.3 |
| 4 | Millers Landing | S | -149.441667 | 60.074167 | 2.3 |
| 5 | LP Fire Department | S | -149.445000 | 60.072500 | 11.2 |
| 6 | Shady Lane | S | -149.439722 | 60.067778 | 1.0 |
| 7 | Fourth of July | O | -149.361944 | 60.083056 | 85.2 |
| 8 | JAG Alaska | S | -149.348056 | 60.085000 | 2.6 |
| 9 | Correctional Center | S | -149.336389 | 60.093056 | 14.2 |
| 10 | Communications North | S | -149.349722 | 60.086944 | 2.9 |
| 11 | Alaska SeaLife Center | S | -149.440000 | 60.099722 | 6.8 |
| 12 | Hospital | S | -149.445833 | 60.104722 | 32.2 |
| 13 | Seward Fire Department | S | -149.440278 | 60.103611 | 18.6 |
| 14 | 3rd Ave and C St | S | -149.441944 | 60.111389 | 5.0 |
| 15 | Cruise Ship Terminal | S | -149.428056 | 60.120000 | 3.0 |
| 16 | The Lagoon | S | -149.441667 | 60.117222 | 1.1 |
| 17 | Seward Marketplace | S | -149.438333 | 60.124167 | 8.2 |
| 18 | Seward Airport | S | -149.414444 | 60.129444 | 1.7 |
| 19 | Seward Hwy and Nash Rd | S | -149.416111 | 60.143889 | 9.0 |
| 20 | Nautical Ave | S | -149.408611 | 60.159722 | 18.2 |
| 21 | Small Boat Harbor | O | -149.435833 | 60.118056 | 2.4 |
| 22 | Harbor entrance | O | -149.432500 | 60.115833 | -1.2 |
| 23 | Tidal gauge | O | -149.426111 | 60.119167 | 9.2 |
| 24 | Seward City Church | S | -149.378333 | 60.130000 | 5.8 |
| 25 | Moose Horn Dr | S | -149.372500 | 60.134444 | 20 |
| 26 | McDonald's Machine Works | S | -149.374444 | 60.128333 | 7.1 |
| 27 | Waterfront Park | S | -149.434167 | 60.106389 | 1.2 |
| 28 | Nash Rd | S | -149.364444 | 60.120556 | 10.6 |

**Table A2.** Maximum water depth for all tsunami scenarios at time series points in Seward.

| # | Location | Max. water depth above ground/sea level (meters) | | | | | | | | | | | | | | | | | |
| | | Scenario | | | | | | | | | | | | | | | | | |
| | | 1 | 2 | 2-PBIE1 | 3 | 4 | 4-PBIE1 | 5 | 6 | 6-PBIE1 | 7 | 7-PBIE1 | 7-PBIE2 | 7-BS | 8 | 8-PBIE1 | 9 | 10 | 11 |
| 1 | Bay entrance | 10.6 | 5.2 | 10.7 | 0.3 | 0.2 | 4.7 | 6.5 | 0.3 | 2.1 | 5.3 | 6.3 | 6.7 | 5.8 | 8.8 | 5.8 | 9.4 | 17.1 | 1.1 |
| 2 | Lowell Point | 18.1 | 7.0 | 16.4 | 0 | 0.7 | 8.1 | 10.9 | 0 | 4.8 | 8.5 | 11.8 | 13.5 | 9.8 | 13.7 | 10.0 | 14.4 | 23.0 | 1.4 |
| 3 | Beach Drive | 16.6 | 5.7 | 15.1 | 0 | 0 | 6.8 | 9.5 | 0 | 3.7 | 7.3 | 10.5 | 12.2 | 8.9 | 12.8 | 8.6 | 13.1 | 21.6 | 0 |
| 4 | Millers Landing | 15.2 | 3.9 | 13.6 | 0 | 0 | 5.5 | 7.9 | 0 | 2.4 | 5.9 | 9.2 | 10.7 | 7.2 | 12.2 | 7.3 | 11.4 | 20.1 | 0 |
| 5 | LP Fire Department | 6.5 | 0 | 4.7 | 0 | 0 | 0 | 0 | 0 | 0 | 0 | 0.6 | 2.1 | 0 | 2.7 | 0 | 2.8 | 11.2 | 0 |
| 6 | Shady Lane | 15.8 | 5.0 | 14.3 | 0 | 0 | 6.0 | 8.7 | 0 | 2.9 | 6.5 | 9.7 | 11.4 | 8.1 | 11.8 | 7.9 | 12.3 | 20.8 | 0 |
| 7 | Fourth of July | 18.3 | 6.7 | 16.4 | 0.1 | 0.6 | 8.0 | 10.9 | 0.1 | 4.8 | 8.4 | 12.2 | 13.5 | 9.6 | 13.9 | 10.1 | 14.4 | 23.2 | 1.4 |
| 8 | JAG Alaska | 16 | 3.6 | 14.1 | 0 | 0 | 5.6 | 8.0 | 0 | 1.5 | 6.0 | 10.0 | 10.7 | 7.2 | 12.3 | 7.7 | 12.4 | 20.7 | 0 |
| 9 | Correctional Center | 7.4 | 0 | 5.1 | 0 | 0 | 0 | 0 | 0 | 0 | 0 | 1.1 | 1.2 | 0 | 3.7 | 0 | 3.7 | 12.3 | 0 |
| 10 | Communications North | 16.0 | 3.4 | 14.0 | 0 | 0 | 5.5 | 7.9 | 0 | 1.4 | 5.9 | 9.9 | 10.8 | 7.4 | 12.1 | 7.9 | 12.4 | 20.7 | 0 |
| 11 | Alaska SeaLife Center | 11.6 | 0 | 10.2 | 0 | 0 | 1.2 | 4.0 | 0 | 0 | 1.8 | 5.2 | 6.6 | 3.1 | 7.8 | 3.2 | 7.8 | 16.7 | 0 |
| 12 | Hospital | 0 | 0 | 0 | 0 | 0 | 0 | 0 | 0 | 0 | 0 | 0 | 0 | 0 | 0 | 0 | 0 | 0 | 0 |
| 13 | Seward Fire Department | 0.2 | 0 | 0 | 0 | 0 | 0 | 0 | 0 | 0 | 0 | 0 | 0 | 0 | 0 | 0 | 0 | 4.9 | 0 |
| 14 | 3rd Ave and C St | 14.6 | 1.9 | 12.8 | 0 | 0 | 4.2 | 6.4 | 0 | 1.2 | 5.1 | 8.7 | 9.1 | 6.2 | 11.7 | 7.1 | 11.7 | 20.1 | 0 |
| 15 | Cruise Ship Terminal | 14.9 | 3.6 | 13.7 | 0 | 0 | 5.6 | 7.9 | 0 | 1.7 | 6.3 | 9.7 | 10.2 | 7.5 | 12.1 | 7.6 | 11.9 | 22.2 | 0 |
| 16 | The Lagoon | 18.2 | 5.8 | 16.7 | 0 | 0 | 8.3 | 10.4 | 0 | 4.5 | 9.1 | 12.9 | 12.9 | 10.6 | 16.3 | 11.0 | 15.5 | 24.2 | 0 |
| 17 | Seward Marketplace | 10.7 | 0 | 8.7 | 0 | 0 | 1.4 | 2.8 | 0 | 0 | 2.1 | 4.3 | 5.0 | 2.5 | 8.7 | 3.8 | 7.5 | 17.8 | 0 |
| 18 | Seward Airport | 20.0 | 6.1 | 18.1 | 0 | 0 | 7.1 | 10.8 | 0 | 3.0 | 7.5 | 11.9 | 14.2 | 8.8 | 14.2 | 9.4 | 15.0 | 24.5 | 0 |
| 19 | Seward Hwy and Nash Rd | 13.0 | 0 | 11.3 | 0 | 0 | 0.5 | 4.1 | 0 | 0 | 1.2 | 5.1 | 7.3 | 2.5 | 7.7 | 2.8 | 8.2 | 16.9 | 0 |
| 20 | Nautical Ave | 10.6 | 0 | 8.1 | 0 | 0 | 0 | 0 | 0 | 0 | 0 | 0.1 | 2.5 | 0 | 4.2 | 0 | 5.0 | 14.9 | 0 |
| 21 | Small Boat Harbor | 20.2 | 7.8 | 18.7 | 0 | 1.0 | 10.1 | 12.5 | 0 | 6.1 | 11.0 | 14.7 | 14.9 | 12.5 | 18.0 | 12.5 | 17.5 | 26.5 | 1.6 |
| 22 | Harbor entrance | 19.4 | 7.8 | 18.1 | 0 | 0.9 | 9.9 | 12.2 | 0 | 5.8 | 10.6 | 14.3 | 14.6 | 12.1 | 16.9 | 12.1 | 16.6 | 25.7 | 1.6 |
| 23 | Tidal gauge | 19.3 | 7.8 | 18.1 | 0 | 1.1 | 9.8 | 12.2 | 0 | 5.8 | 10.5 | 14.1 | 14.6 | 11.8 | 16.4 | 11.9 | 16.3 | 26.3 | 1.6 |
| 24 | Seward City Church | 19.1 | 2.6 | 16.7 | 0 | 0 | 3.2 | 9.6 | 0 | 0 | 4.0 | 11.6 | 13.0 | 7.1 | 15.3 | 7.6 | 14.7 | 22.7 | 0 |
| 25 | Moose Horn Dr | 6.8 | 0 | 5.2 | 0 | 0 | 0 | 0 | 0 | 0 | 0 | 0 | 1.0 | 0 | 1.6 | 0 | 2.5 | 10.5 | 0 |
| 26 | McDonald's Machine Works | 17.2 | 0.5 | 14.6 | 0 | 0 | 2.6 | 7.2 | 0 | 0.6 | 3.2 | 9.0 | 11.2 | 4.6 | 12.9 | 6.3 | 12.4 | 21.2 | 0 |
| 27 | Waterfront Park | 17.7 | 5.3 | 16.1 | 0 | 0 | 7 | 9.8 | 0 | 3.4 | 7.8 | 11.6 | 12.5 | 9.0 | 13.6 | 9.3 | 14.0 | 22.8 | 0 |
| 28 | Nash Rd | 10.0 | 0 | 7.1 | 0 | 0 | 0 | 1.2 | 0 | 0 | 0 | 3.4 | 3.8 | 0.9 | 5.2 | 1.4 | 5.4 | 16.1 | 0 |

**Table A3.** Maximum water velocities for all tsunami scenarios at time series points in Seward.

| # | Location | Max. water velocity (meters/second) Scenario | | | | | | | | | | | | | | | | | |
|---|---|---|---|---|---|---|---|---|---|---|---|---|---|---|---|---|---|---|---|
| | | 1 | 2 | 2-PBIE1 | 3 | 4 | 4-PBIE1 | 5 | 6 | 6-PBIE1 | 7 | 7-PBIE1 | 7-PBIE2 | 7-BS | 8 | 8-PBIE1 | 9 | 10 | 11 |
| 1 | Bay entrance | 2.9 | 1.9 | 2.2 | 0.5 | 1.5 | 1.8 | 2.5 | 0.5 | 1.3 | 3.2 | 2.4 | 2.4 | 3.4 | 2.9 | 2.4 | 2.5 | 4.2 | 0.3 |
| 2 | Lowell Point | 2.5 | 1.1 | 1.7 | 0.3 | 0.6 | 1.4 | 1.7 | 0.3 | 1.1 | 1.9 | 1.8 | 1.8 | 2.1 | 2.6 | 2.0 | 2.4 | 3.5 | 0.2 |
| 3 | Beach Drive | 3.7 | 1.2 | 2.6 | 0 | 0 | 2.3 | 2.5 | 0 | 1.6 | 2.4 | 4.2 | 3.8 | 2.8 | 3.6 | 5.6 | 2.9 | 4.8 | 0 |
| 4 | Millers Landing | 4.2 | 1.9 | 3.9 | 0 | 0 | 2.6 | 2.3 | 0 | 2.5 | 2.2 | 5.6 | 4.9 | 2.7 | 4.3 | 6.4 | 4.2 | 4.4 | 0 |
| 5 | LP Fire Department | 7.0 | 0 | 7.4 | 0 | 0 | 0 | 0 | 0 | 0 | 0 | 4.5 | 5.4 | 0 | 8.4 | 0 | 5.6 | 7.3 | 0 |
| 6 | Shady Lane | 3.4 | 1.4 | 2.8 | 0 | 0 | 2.8 | 2.1 | 0 | 2.6 | 2.1 | 3.6 | 3.4 | 2.9 | 4.0 | 4.3 | 2.6 | 3.7 | 0 |
| 7 | Fourth of July | 1.7 | 0.8 | 1.3 | 0.2 | 0.4 | 1.0 | 1.2 | 0.2 | 0.7 | 1.3 | 1.2 | 1.2 | 1.5 | 1.7 | 1.3 | 1.6 | 2.6 | 0.1 |
| 8 | JAG Alaska | 5.2 | 2.0 | 4.7 | 0 | 0 | 3.6 | 3.2 | 0 | 2.3 | 3.8 | 5.1 | 4.2 | 4.1 | 5.3 | 4.2 | 4.7 | 5.4 | 0 |
| 9 | Correctional Center | 5.0 | 0 | 4.3 | 0 | 0 | 0 | 0 | 0 | 0 | 0 | 1.9 | 1.9 | 0 | 5.0 | 0 | 4.1 | 4.4 | 0 |
| 10 | Communications North | 6.1 | 2.4 | 5.3 | 0 | 0 | 4.0 | 3.8 | 0 | 2.2 | 3.9 | 5.6 | 5.2 | 4.6 | 6.0 | 4.7 | 5.0 | 5.1 | 0 |
| 11 | Alaska SeaLife Center | 10.5 | 0 | 3.5 | 0 | 0 | 1.7 | 2.2 | 0 | 0 | 2.4 | 4.2 | 2.1 | 2.5 | 3.6 | 4.4 | 3.9 | 9.3 | 0 |
| 12 | Hospital | 0 | 0 | 0 | 0 | 0 | 0 | 0 | 0 | 0 | 0 | 0 | 0 | 0 | 0 | 0 | 0 | 0 | 0 |
| 13 | Seward Fire Department | 0 | 0 | 0 | 0 | 0 | 0 | 0 | 0 | 0 | 0 | 0 | 0 | 0 | 0 | 0 | 0 | 10.4 | 0 |
| 14 | 3rd Ave and C St | 5.0 | 3.6 | 4.5 | 0 | 0 | 2.0 | 2.0 | 0 | 4.3 | 2.0 | 3.2 | 4.3 | 3 | 5.0 | 5.4 | 4.0 | 4.2 | 0 |
| 15 | Cruise Ship Terminal | 24.8 | 8.4 | 20.9 | 0 | 0 | 10.9 | 48.6 | 0 | 5.4 | 11.5 | 38.3 | 53.1 | 19.4 | 19.1 | 26.0 | 21.8 | 18.3 | 0 |
| 16 | The Lagoon | 5.3 | 4.1 | 4.8 | 0 | 0 | 5.1 | 4.2 | 0 | 4.0 | 4.0 | 5.1 | 5.0 | 4.9 | 6.8 | 5.8 | 5.1 | 5.7 | 0 |
| 17 | Seward Marketplace | 6.7 | 0 | 5.9 | 0 | 0 | 3.4 | 3.2 | 0 | 0 | 3.6 | 6.5 | 5.5 | 5.7 | 7.1 | 6.7 | 5.6 | 6.3 | 0 |
| 18 | Seward Airport | 10.5 | 4.5 | 9.7 | 0 | 0 | 6.8 | 7.0 | 0 | 4.5 | 6.7 | 9.3 | 8.8 | 7.9 | 10.7 | 8.0 | 9.5 | 12.5 | 0 |
| 19 | Seward Hwy and Nash Rd | 14.4 | 0 | 13.7 | 0 | 0 | 1.4 | 26.3 | 0 | 0 | 4.4 | 15.5 | 11.6 | 7.0 | 12.7 | 10.6 | 12.9 | 12.7 | 0 |
| 20 | Nautical Ave | 9.4 | 0 | 7.9 | 0 | 0 | 0 | 0 | 0 | 0 | 0 | 0 | 2.6 | 0 | 6.1 | 0 | 6.4 | 8.2 | 0 |
| 21 | Small Boat Harbor | 3.7 | 1.2 | 3.8 | 0.7 | 1.2 | 2.4 | 1.9 | 0.7 | 2.4 | 2.1 | 3.7 | 3.4 | 2.8 | 4.2 | 3.8 | 3.6 | 4.4 | 0.6 |
| 22 | Harbor entrance | 13.6 | 10.6 | 11.4 | 20.3 | 24.3 | 19.8 | 11.3 | 20.3 | 21.2 | 19.4 | 21.6 | 22.5 | 18.5 | 11.5 | 11.5 | 8.5 | 16.3 | 4.8 |
| 23 | Tidal gauge | 5.9 | 1.5 | 5.2 | 0.3 | 0.5 | 4.7 | 4.7 | 0.3 | 3.3 | 4.7 | 5.5 | 5.7 | 5.1 | 5.3 | 5.6 | 5.3 | 7.4 | 0.1 |
| 24 | Seward City Church | 6.0 | 2.5 | 6.4 | 0 | 0 | 4.8 | 3.7 | 0 | 0 | 5.0 | 6.4 | 5.7 | 4.9 | 7.4 | 8.0 | 5.0 | 5.6 | 0 |
| 25 | Moose Horn Dr | 6.7 | 0 | 5.8 | 0 | 0 | 0 | 0 | 0 | 0 | 0 | 0 | 1.8 | 0 | 3.3 | 0 | 4.1 | 2.7 | 0 |
| 26 | McDonald's Machine Works | 7.9 | 2.8 | 5.9 | 0 | 0 | 3.9 | 4.7 | 0 | 1.2 | 4.8 | 6.9 | 6.4 | 5.9 | 8.2 | 6.8 | 6.7 | 5.5 | 0 |
| 27 | Waterfront Park | 6.3 | 1.0 | 6.2 | 0 | 0 | 2.1 | 3.9 | 0 | 1.2 | 2.8 | 4.1 | 7.4 | 3.4 | 8.3 | 5.0 | 6.0 | 7.0 | 0 |
| 28 | Nash Rd | 9.2 | 0 | 8.9 | 0 | 0 | 0 | 2.0 | 0 | 0 | 0 | 3.4 | 4.9 | 2.1 | 6.0 | 3.0 | 6.3 | 6.6 | 0 |